Journal of Geophysical Research: Space Physics

RESEARCH ARTICLE
10.1029/2017JA025085

Key Points:
- Data show an enhancement in the ratio between ions with mass per charge equal to 2 and protons in the dusk sector
- Enhancement is independent of the location of the moons with respect to the spacecraft and of season
- Plasma stagnation point occurs at earlier local time than suggested by previous modeling

Correspondence to:
M. Felici,
mfelici@bu.edu

Citation:
Felici, M., Arridge, C. S., Wilson, R. J., Coates, A. J., Thomsen, M., & Reisenfeld, D. (2018). Survey of thermal plasma composition in Saturn's magnetosphere using time-of-flight data from Cassini/CAPS. *Journal of Geophysical Research: Space Physics*, *123*. https://doi.org/10.1029/2017JA025085

Received 2 DEC 2017
Accepted 21 JUL 2018
Accepted article online 1 AUG 2018

Survey of Thermal Plasma Composition in Saturn's Magnetosphere Using Time-of-Flight Data From Cassini/CAPS

M. Felici[1], C. S. Arridge[2], R. J. Wilson[3], A. J. Coates[4], M. Thomsen[5], and D. Reisenfeld[6]

[1]Center for Space Physics, Boston University, Boston MA, USA, [2]Lancaster University, Lancaster, UK, [3]Laboratory for Atmospheric and Space Physics, Boulder, CO, USA, [4]Mullard Space Science Laboratory, University College London, London, UK, [5]Planetary Science Institute, Tucson, AZ, USA, [6]University of Montana, Missoula, MT, USA

Abstract The Cassini spacecraft orbited Saturn from 2004 to 2017, and in 2006 it started exploring the deep magnetotail, reaching distances of about 68 R_S (where R_S is the equatorial radius of Saturn). Since Cassini covered a broad area of Saturn's magnetosphere, this raises the question of what is the typical and atypical plasma composition in different regions of Saturn's environment. In this paper, we present a survey of the bulk plasma composition using time-of-flight data from the Plasma Spectrometer/Ion Mass Spectrometer instrument on Cassini, from 2004 through 2012. This is the most comprehensive study ever made of relative abundances of thermal plasma at Saturn, maximizing the use of Cassini's orbital coverage in Saturn's magnetosphere during those years, and, therefore, the sensitivity to seasonal or natural variability of the system. We studied the ratio of counts between ions with $E/q \simeq 1.19–21{,}300$ eV/q and mass per charge equal to 2 (either H_2^+ or He^{++}) and ionized hydrogen ($[(m/q = 2)]/[H^+]$), and a mixture of ions (H_2O^+, H_3O^+, OH^+, and O^+), known as the water group (W^+) and ionized hydrogen ($[W^+]/[H^+]$). We present the data as a function of position in the magnetosphere, radial distance and local time, and distance from the planet and longitude with respect to the moons Enceladus, Dione, Rhea, and Titan. We found that the plasma composition in Saturn's magnetosphere presents significant local time asymmetries and variability.

1. Introduction

The aim of this study is to provide a global picture of low-energy plasma composition in Saturn's magnetosphere. This aim is accomplished by a comprehensive plasma survey that uses time-of-flight (TOF) data from the Cassini plasma spectrometer/ion mass spectrometer (CAPS/IMS) instrument. Data from the entire on-orbit lifetime of the CAPS/IMS instrument are used (2004 through 2012). The motivating factors for this study are to improve constraints on plasma circulation patterns, to identify more clearly plasma sources and sinks, and to provide a more general description of Saturn's magnetosphere. This study builds upon previous works in this area including, for example, Andriopoulou et al. (2012, 2014), Wilson et al. (2013), and Thomsen et al. (2010, 2014).

1.1. Plasma Sources

Multiple species and multiple sources, internal and external to the magnetosphere, contribute to Saturn's plasma system.

Sittler et al. 2008 use ion-electron fluid parameters derived from CAPS observations within Saturn's inner magnetosphere and consider in their model both transport and ion recombination (dependent on electron density and thermal electron temperature) as a function of *L*: They find that recombination dominates inside Dione's L shell, whereas transport dominates outside Dione's L shell. They find that the ion production (proton and water group together) maximum is 10^{27} ions per second, and it varies radially peaking at Tethys and Dione; they see no peak at Enceladus' L shell. They also find that the production of neutral molecules, instead, peaks near Enceladus' with a value of 2×10^{28} mol/s, value in the range of previous estimates (e.g., Fleshman et al., 2013; Hansen et al., 2006; Jurac et al., 2002; Richardson & Jurac, 2004; Tokar et al., 2006; Waite et al., 2006). Paranicas et al. (2012) find that the dominant Energetic Neutral Atoms (ENA) signal is found near the orbit of Rhea.

Saturn's main rings are a source of H_2^+, O^+, and O_2^+ (Bouhram et al., 2006; Johnson, Luhmann, et al., 2006; Johnson, Smith, et al., 2006; Luhmann et al., 2005; Martens et al., 2008; Tokar et al., 2005; Tseng et al., 2010). Using a photochemical model and CAPS data, Elrod et al. (2012) demonstrated that production of neutrals from Saturn's ring atmosphere changes seasonally, influencing the ring plasma overtime. Tseng et al. (2013) model a source rate for H_2 due to photolysis of 2.0×10^{26} s^{-1} and for O_2 of 2.0×10^{27} s^{-1} (corrected for the amount of oxygen from Enceladus deposited in the A ring) at Saturn Orbit Insertion (SOI), and for H_2 due to photolysis of 2.0×10^{24} s^{-1} and for O_2 of 2.0×10^{25} s^{-1} at equinox: Once ionized, these molecules contribute to the local magnetospheric plasma. The spatial overlap between the E ring and Enceladus and also between Mimas and the G ring complicates the differentiation between satellite and ring sources or absorption.

For Titan, Johnson et al. (2010) estimate a total ion loss rate of $1–5 \times 10^{26}$ amu/s. Coates et al. (2012) used observations of Cassini/CAPS electron and ion TOF spectra collected crossing Titan's tail and estimated a loss rates of 8.9, 1.6, and 4.0 $\times 10^{25}$ amu/s for three crossings of Titan's tail.

Plasma produced in the inner magnetosphere is transported to the outer magnetosphere (on time scales of weeks) via centrifugally driven interchange instability (Mauk et al., 2009, and references therein). One strong signature of this process is the injection of hot plasma into the inner magnetosphere, associated with magnetic pressure enhancements or deficits (e.g., André et al., 2005, 2007; Hill et al., 2005; Thomsen, 2013).

Felici et al. (2016) report a case study of Cassini data from Saturn's magnetotail, when the spacecraft was located at ≃2200 LT at 36 R_S from Saturn. They interpreted this event as detection of ionospheric outflow in Saturn's magnetotail and estimated that the ionosphere could potentially provide a quantity of mass between 1.4×10^2 and 1.1×10^3 kg/s to the system, although it is not clear how much of this mass remains within the magnetosphere and how much is lost to the solar wind.

To obtain a rough estimate of the contribution of the solar wind a source of plasma for Saturn's magnetosphere we can multiply the solar wind mass flux $n_{SW}v_{SW}$ by the cross-sectional area of the magnetosphere: $n_{SW}v_{SW}\pi R_0^2$. Estimating a magnetopause of cross-sectional area $\pi(30\ R_S)^2$ (terminator radius of the magnetopause from Kanani et al., 2010), considering a solar wind number density between 0.002 and 0.4 cm^{-3}, a solar wind speed between 400 and 600 km/s (Crary et al., 2005), and an efficiency factor $O(10^{-3})$ (Bagenal & Delamere, 2011; Hill, 1979; Hill et al., 1983; Vasyliunas, 2008) to account for the portion of plasma that does not make it in the magnetosphere, we obtain an upper limit for the plasma provided by the solar wind to Saturn's magnetosphere: 8.21×10^{24} to 2.46×10^{27} ions per second.

1.2. Plasma Flow

In terms of circulation patterns, the interaction of the solar wind with the magnetosphere and the magnetospheric plasma motion caused by the planet rotation cause a total electric potential in the equatorial plane given by the sum of the convection and corotation potentials. However, the corotation potential decreases with distance, so, at large distances, the convection potential will dominate the drift of the cold plasma. This creates two different regions in the magnetosphere. The first region is close to the planet and presents closed equipotential field lines; corotation dominates; and the content of a flux tube is practically constant (*plasmasphere*). Out of this region, the electric field has a very strong duskward component and the flux tubes are destined to encounter the dayside magnetopause and lose their plasma to the magnetosheath. Therefore, the plasma density in this region drops from that in the plasmasphere. The point where the equipotential field lines intersect at dusk is called the stagnation point. When the solar wind arrives at Saturn, the dynamic pressure and the magnetic field are much weaker than around Earth, potentially implying that solar wind effects on Saturn's magnetospheric dynamics are somehow secondary to internally driven dynamics. However, the main auroral oval has been observed to undertake dramatic changes in response to the detected solar wind disturbances, such as coronal mass ejections and corotating interaction regions (Badman & Cowley, 2007; Cowley et al., 2004). Therefore, Dungey's (1961) and Vasyliunas's (1983) convection patterns have been hypothesized to work together in Saturn's system (Cowley et al., 2004). Dungey (1961) hypothesized that the interplanetary magnetic field control is exerted by the reconnection phenomenon, consisting of the linking between interplanetary and planetary magnetic field; magnetic flux is then carried into the nightside magnetosphere where it builds up until reconnection happens in the tail. Reconnection in the Dungey cycle (Dungey, 1961), namely, reconnection of open field lines carrying solar wind plasma, is then constrained in the postmidnight sector; the X line, in this case, is located tailward from the region of returning flux from Vasilyunas cycle, and the reconnected lobe flux tubes move sunward along the dawn flank. While the Dungey cycle is driven by interaction with the solar wind and involves reconnection of open field lines, the Vasyliunas

cycle is internally driven and involves reconnection of closed field lines loaded with plasma (Vasyliunas, 1983). Reconnection in the Vasyliunas cycle (Vasyliunas, 1983), namely, centrifugally driven reconnection of closed flux tubes loaded with magnetospheric plasma, is mostly restricted to the premidnight sector: These flux tubes stretch in this area of the magnetosphere, preventing Dungey cycle reconnection from happening in that region. This kind of reconnection allows plasma loss downtail, and the reconnected and plasma depleted flux tubes, then, return to a more dipolar configuration through the postmidnight sector.

McAndrews et al. (2009) found tailward flows in the postmidnight plasma sheet containing water group ions (W^+)—composition different from that expected for a Dungey cycle—and not northward magnetic field—opposite to that expected for a region located after Dungey or Vasyliunas reconnection lines. Results from Thomsen et al. (2014) are consistent with McAndrews et al. (2009), namely, they found that the ionosphere has a strong influence on the flow, but beyond 20 R_S the magnetic field is not strong enough to bring the circulating plasma to the dayside and there is a radial mass outflow. They find a clear mass outflow beyond 30 R_S in the dusk sector, in a direction parallel to the dusk magnetopause, consistent with a dusk *wing* (Delamere et al., 2013; Jia et al., 2012).

The simulations of Jia et al. (2012) find results, for the relative location of reconnection sites and convection pattern, generally consistent with Cowley et al. (2004), having then an interplay between the two cycles in Saturn's system. They estimated that all plasma from Enceladus and other internal plasma sources cannot be removed from the system only by large scale plasmoids and that a large fraction of the plasma is lost through the flanks of the tail by possibly small-scale plasmoids. Cowley et al. (2015) estimate, however, that the downtail plasma loss via plasmoids was underestimated by an order of magnitude and that, actually, this mechanism might be sufficient at both Jupiter and Saturn, to lose material loaded in the magnetosphere by Io and Enceladus, respectively. At Saturn, Hill et al. (2008) present a study on three plasmoids, two of which had sufficient plasma to determine ion composition, which was dominated by water group ions, indicating an inner magnetosphere source. Smith et al. (2016) observed that the reconnection rate at Saturn peaks in the postmidnight sector, although on the dusk flank there is a more sporadic yet steady loss.

Jia and Kivelson (2016) simulate plasma and field properties of the near-equatorial regions between $L = 5$ and 10. They find agreement with previous finding but also interpret the net flow from dusk to dawn. The way in which the plasma is distributed along flux tubes, while the flux tubes rotate around the planet, is controlled by the balance of the centripetal term and the pressure gradient force. In the postmidnight quadrant, the field is stretched by both pressure gradient and centripetal terms. The field-aligned component of the centripetal term is large, and the plasma is confined near the equator, producing a thin plasma sheet. When the dipolarizing flux tube rotates toward dawn, the plasma flows away from the equator, as the dipolarization reduces the effect of the centripetal term, so the plasma can expand along the flux tube. Hence, the plasma sheet thickens again. The flux tubes then rotate from noon toward dusk, but the plasma does not return to the equator straight away because the field-aligned component of the centripetal term is small near the equator along a dipolar filed line.

McComas et al. (2017) analyze plasma observations from New Horizons, collected when the spacecraft was going from 600 R_J to distances larger than 2,500 R_J through the dusk flank of the Jovian magnetotail. They find that light ions dominate over the heavy ions, contrary of what is observed near Jupiter's plasma disk. They suggest a few mechanisms to explain these observations: The heavy ions are confined in the plasma sheet and the spacecraft might have passed above it, or internal (ionosphere) or external (solar wind) sources of light ions might be stronger than Io (source of heavy ions); McComas et al. (2017) add that another explanation for their observations: as possible consequence of the fact that, whereas the plasma disk generally retains the heavy ions while the flux tubes rotate through dusk and the midnight sector, the flux tubes are increasingly bent back until they reach the dawn flank (Khurana, 2001; Kivelson & Southwood, 2005), then heavy ions are released in the downside of the tail, allowing the flux tubes return radially to fit the downside magnetosphere.

In the model of Jupiter by Delamere and Bagenal (2010) the plasma beyond 60 R_J can reach sink regions at the dawn magnetopause, and, along the magnetopause, the viscous solar wind interaction via Kelvin-Helmholtz vortices allows the exchange of mass and momentum with the magnetospheric plasma. Delamere et al. (2013) extended this model showing region of closed flux along the dawn and dusk flanks, where there is interaction with the solar wind. Krimigis et al. (2005), using the Magnetospheric Imaging Instrument on Cassini, measured the energetic ion population upstream from the sides of Saturn's magnetosphere. They find upstream energetic hydrogen and oxygen ions up to distances of 120 R_S, that they interpret as ions leaked from Saturn's

magnetosphere when the interplanetary magnetic field is in a favorable configuration. Thomsen et al. (2007), used CAPS data on Cassini to study the composition of the ions with E/q between 3 and 50 keV/q located upstream from Saturn's bow shock. They find that the ion composition is given by H^+ and ions with ($m/q = 2$), which they suggest being solar wind He^{++} but no magnetospheric water group ions: They suggest that leaks from the magnetosphere may not be a significant source of upstream ions in that energy range.

1.3. Asymmetries of the Magnetosphere

The instantaneous magnetospheric tilt, the net tilt angle between the dipole equator and the solar wind, is a function of planetary rotational and orbital phase. Depending on the planet's obliquity and dipole tilt, we have a spectrum of periodicities for every different magnetized planet (Arridge et al., 2008). When the dipole magnetic equator is not perpendicular to the solar wind flow, the solar wind exerts a normal stress on the current sheet and, beyond compressing the dayside and stretching the nightside, shifts the location of the magnetic equator (Arridge et al., 2008): The magnetospheric current sheet is moved northward (southward) over all local times (LTs) for negative (positive) magnetospheric tilt angles. The data confirm the model of Arridge et al. (2008).

From the comparison between two passes of identical geometry from January 2007 (with Cassini crossing the equatorial plane in the postmidnight sector at a distance of $\simeq 21 R_S$) and two passes from April 2009 (also of identical geometry, with Cassini crossing the equatorial plane in the premidnight sector again at a distance of $\simeq 21 R_S$) a change in the tilt and vertical offset of the planetary nightside plasma sheet was observed (Sergis et al., 2011). The plasma sheet becomes more and more aligned to the solar wind direction reaching the Saturnian equinox (August 2009). The scale height of the plasma species was found directly proportional to the temperature and inversely proportional to the mass of the particle ($\propto \sqrt{T/m}$); thus, the thickness of the plasma sheet is energy and mass dependent (Hill & Michel, 1976) and becomes more complex in a multispecies plasma.

In the Jovian and Kronian magnetospheres additional asymmetries were observed. At Jupiter, beyond $\simeq 20\ R_J$, the plasma sheet is 10 times thicker at dusk ($\simeq 20\ R_J$) than at dawn ($\simeq 2\ R_J$; (Lanzerotti et al., 1993).

At Saturn, asymmetries caused by an electric field from noon to midnight were observed, corresponding to a radially inward flow in the afternoon and a radially outward flow in the morning within 10 R_S (Andriopoulou et al., 2012; Thomsen et al., 2012; Wilson et al., 2013). Pilkington et al. (2015) find an additional dawn-dusk asymmetry in the magnetosphere, which extends farther from the planet on the dawnside of the planet by $7 \pm 1\%$. Krimigis et al. (2007) show that higher pressures on the dayside extend to much higher latitudes compared to the nightside, more evidently for distances $<20\ R_S$, suggesting that the plasma sheet in the dayside is thicker than in the nightside.

1.4. Low- and High-Energy Ion Composition at Saturn

Thomsen et al. (2010), who presented the first survey of thermal plasma, have restricted attention to low latitudes (within $\pm 5°$ of the equatorial plane) and to when corotation is covered in the CAPS field of view. The study shows that the density of $m/q = 2$ follows H^+ density fairly well, from several percent in the inner magnetosphere to several tens of percent in the outer magnetosphere and tail (Thomsen et al., 2010). Farther than 17 R_S, they measured a bimodal distribution of values, indicating that the lower values of the ratio correspond to magnetosheath/solar wind, whereas the higher values are given by inner magnetosphere plasma. This suggests that the solar wind is not the main source of plasma for the outer magnetosphere. The enhancement in the relative density $[(m/q = 2)]/[H^+]$ around 20 R_S suggests that Titan is an important source of H_2^+. Tseng et al. (2011) modeled the trend of H_2^+ source rate in the magnetosphere. H_2^+ is produced from H_2 through photoionization, electron impact ionization, and charge exchange with magnetospheric plasma ions, and they showed that the ionization source rate peaks at the rings, at Rhea, and at Titan, matching the peaks measured by Thomsen et al. (2010).

DiFabio et al. (2011), DiFabio (2012), and Blanc et al. (2015) use the Charge Energy Mass Spectrometer (CHEMS) on Cassini to study long-term time variations of the ions with E/Q in the range 27–220 keV/q, and they find $[H_2^+]/[H^+]$ partial number densities ratios for $L = 7$–16 to be 0.1 and $[H^{++}]/[H^+]$ to be 0.0029, and the latter ratio reaches a value of 0.0074 for $L = 15$–21. DiFabio et al. (2011) also find that the solar wind ions He^{++} decrease significantly near solar minimum (2009–2010). Blanc et al. (2015) estimate from results from DiFabio et al. (2011) that 84% of the magnetospheric H^+ originated in the magnetosphere, and the rest comes from the solar wind.

Thomsen et al. (2010) also studied the relative density $[W^+]/[H^+]$ variability with distance: They found that W^+ dominates over H^+ on the equatorial plane, and they found a peak around Titan, which is not expected from models (e.g., Johnson et al., 2010). Persoon et al.'s (2009) model shows that the heavier ions are closely confined to the equatorial plane in the inner magnetosphere, and the equatorial density profile of W^+ peaks at 4.8 R_S. Reisenfeld et al. (2008) also used TOF data from CAPS/IMS. Their data cover 2 years, predominantly in the region of the dawn magnetosphere. They found that W^+ ions dominate over H^+ up to 25 R_S, but W^+ ions are detected till 36 R_S.

Wilson et al. (2015) studied relative abundances of W^+ ions in the inner magnetosphere over two orbits in 2011. They find that different W^+ species dominate in different regions and also have different dependencies with radial distance: H_2O^+ is the dominant W^+ species between 4.75 and 8 R_S, whereas OH^+ dominates between 8 and 10 R_S. H_3O^+ is the second dominant species between 4.75 and 6.25 R_S, whereas OH^+ is the second dominant species between 6.25 and 8 R_S and H_2O^+ is between 8 and 10 R_S. O^+ is the least dominant species from 4.75 to 8.25, and then H_3O^+ is the least dominant one after that. H_3O^+ abundance decreases dramatically with increasing distance from Saturn, whereas H_2O^+ diminishes more smoothly and OH^+ and O^+ instead increase with radial distance up to 10 R_S.

DiFabio et al. (2011), DiFabio (2012), and Blanc et al. (2015), using CHEMS data, find the relative density $[W^+]/[H^+]$ to be 2.1 in the range $L = 7-16$.

Holmberg et al. (2012) use the Radio and Plasma Wave Science Langmuir probe to map the ion density of Saturn's inner plasma torus. They use data from 129 orbits and find that the main plasma torus is located between 2.5 and 8 R_S from the planet, with the ion density that reaches its maximum between the orbits of Enceladus and Tethys. Holmberg et al. (2014) use the Radio and Plasma Wave Science Langmuir probe measurements from 129 Cassini orbits and find higher ion density values at the nightside and lower values at the dayside, confirming a day/night asymmetry, and from their Figure 1b, we can appreciate how the ion density is more radially extended at dusk. Holmberg et al. (2017) use the Radio and Plasma Wave Science Langmuir probe to map Saturn's plasma disk between 2.5 and 12 R_S, and they find that the plasma density peak is located at $\simeq$4.6 R_S, not near the main neutral source region (Enceladus) at 3.95 R_S, due to the fact that ionization rate by the hot electron impact peaks at $\simeq$4.6 R_S. They also confirm the result found in Holmberg et al. 2014: A dayside/nightside ion density asymmetry, where the densities in the nightside are found to be up to a factor of 2 larger than the densities on the dayside, especially in the region between 4 and 5 R_S from the planet.

1.5. In This Paper

In this paper, in sections 2 and 3 we describe the data reduction process that was designed and implemented in order to minimize all the possible biases given by differences in the way that the data are collected, packed, and transmitted to Earth. Subsequently, we will describe how the fits were performed to give the ion counts associated with various species and further filters that were applied to the data. We will then illustrate the data analysis performed on the results of the fits, before the data were plotted. Lastly, we will present and discuss our results, for relative counts $[(m/q = 2)]/[H^+]$ and $[W^+]/[H^+]$, since H^+, H_2^+, and W^+ are the three most abundant species in Saturn's magnetosphere. We will present our results in different ways:

1. in the *X*-*Y* and *Y*-*Z* planes in Kronocentric Solar Magnetic (KSMAG) coordinate system (Arridge et al., 2008), also separated seasonally by solstices and equinox;
2. in cylindrical coordinate system showing ratios versus distance from Saturn and LT sector;
3. as ratios versus distance from Saturn and longitude of the spacecraft with respect to Enceladus, Dione, Rhea, and Titan.

2. Instrumentation

The CAPS measures the energy per charge and arrival direction of electrons and ions. The instrument consists of three sensors: the electron spectrometer (ELS), which measures electrons from 0.7 eV/q to 29 keV/q, the ion beam spectrometer (IBS), which measures narrow ion beams from 1 eV/q to 50 keV/q, and the IMS, formed by a top hat electrostatic analyzer that measures the E/q of ions in the range from 1 eV/q to 50 keV/q (SNG data), followed by a TOF analyzer for the determination of mass per charge of incoming particles. A motor-driven actuator rotates the sensor package to provide a useful range restricted in azimuth to $-80° < \psi < +104°$ scanning in the azimuth of the spacecraft, covering approximately 2π sr of the sky every 3 min; the spacecraft rolls can occasionally increase the field of view to 4π sr (Young et al., 2004).

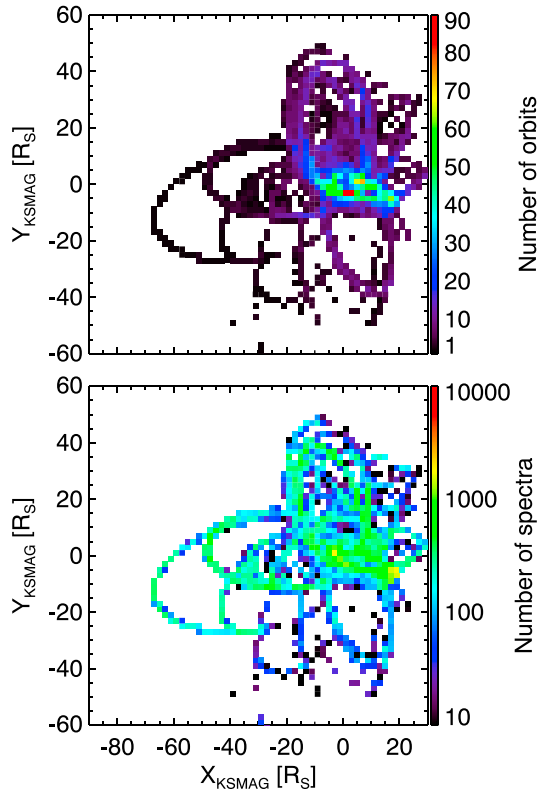

Figure 1. Number of orbits (top) and number of time-of-flight spectra (bottom) binned in 2 $R_S \times 2$ R_S bins in the equatorial plane (X-Y in KSMAG coordinate system). Both the number of orbits per bin (top) and number of time-of-flight spectra (bottom) are summed in Z and collapsed together in the same bin in X-Y. In the plots, Saturn is located at the origin, dayside is on the positive X direction on the right, in the positive Y direction we find the dusk sector, midnight is on the left, and dawn sector is at the bottom of the plot. KSMAG = Kronocentric Solar Magnetic.

IMS does not identify ion mass separately. After the ions exit the top hat they pass through a carbon foil, liberating an electron that generates a start signal. The stop signal for the TOF is generated by the ion or its neutral counterpart. The start-only signals (called singles data, SNG) are monitored separately from the coincidence (start and stop) signals that make the TOF data set. SNG data carries the information of the direction of motion of detected particles. TOF data instead do not carry any directional information.

The top hat analyzer covers the whole E/q range, adjusting the potential difference between the two curved plates of the electrostatic analyzer every 4 s, in 64 intervals (63 measured energies and 1 fly back). The accumulation time is 62.5 ms for each voltage, but one eighth of this, 7.8125 ms, is dead time used to switch to the next voltage; therefore, the real accumulation time is 54.6875 ms for each of the 63 steps. TOF, instead, has 32 energy steps rather than 63. In the case of IMS, the term azimuth refers to a particular voltage sweep of the top hat analyzer from high to low voltages (energy step 1 to energy step 63). The sweep tables report the correct value of the voltage steps over the hemispheres of the top hat and/or the corresponding E/q of the ions selected by those voltage steps used in the instrument during a specific data acquisition.

An A cycle is the basic interval of time for the CAPS instruments and lasts 32 s. For SNG data, a complete voltage sweep lasts 4 s, as such there are eight voltage sweeps (the electrostatic analyzer goes through the 63 energy steps) per A cycle. B cycles are instead used for TOF measurements. A B cycle, theoretically, can have one of three different durations, usually 256 s, but also 512 or 1,024 s (8, 16, or 32 A cycles), dependent on telemetry modes. However, only a subset of the daily A cycles are also included in B cycles, which is dependent on the telemetry mode of the time.

The TOF instrument has 2,048 different TOF channels (1 TOF channel = 0.78125 ns) where data can fall, but only a subset are returned to Earth. At most 512 TOF channels are returned. Even if 512 channels are present in the TOF data product, they do not necessarily correspond to the same subset of 2,048 channels. From SOI up until 2005-058T01:00:00, the 512 channels corresponded to every fourth channel of the full 2048, for both the straight-through (ST; TOF) detector and linear electric field detector (LEF; TOF). After 2005-058T01:00:00 the start channel is number 40, with every other channel returned, continuing up to channel 1062.

In this study we use data from the ST detector.

3. Methods

We chose to study the variability of the ratio of counts between species to automatically eliminate the bias that would have been introduced by having areas of the magnetosphere covered multiple times by the spacecraft, possibly resulting in more counts in specific regions than in others.

In this study we use ratio between counts, $[(m/q = 2)]/[H^+]$ and $[W^+]/[H^+]$, and not purely counts for each species, for the following reasons:

1. The spacecraft spent different amounts of time in different regions of the magnetosphere (see Figure 1), so if we wanted to use counts for this study, in each bin we should have had to renormalize the counts for each species by the average number of counts for that species in that bin.
2. If we had renormalized the counts, however, as mentioned in the previous point, the average number of counts would have been biased by the fact that the environmental conditions, and look directions, are different for each passage in a bin; in fact, the CAPS actuator can be off (*staring* mode) or on, but, even in the latter case, the instrument does not have full sky viewing and covers only 2π steradians: If the instrument

is not looking in the right direction, ion beams can be missed. To solve that, we could have filtered the data by look direction, but TOF data do not carry directional information.
3. To obtain directional information, we could have utilized SNG data (which carries directional information) to select a look direction, but doing so, we should have excluded valuable information (e.g., data collected when CAPS was looking in a different direction from the one selected) from this study that, instead, wants to give a global picture of Saturn's magnetosphere.

This study may also contribute to the identification of areas with solar wind influence (known values for this relative density $[He^{++}]/[H^+]$ peaks at ≃4%, but can reach ≃7–8%, in the solar wind (Kasper et al., 2007; Wang, 2008), and to better understand the correlation between species. From Blanc et al. (2015, and references therein) we know that, at higher energies, $H_2^+/H^+ \simeq 0.17$, whereas $He^{++}/H^+ \simeq 0.0029$ in the inner magnetosphere, and we expect high relative counts $[(m/q = 2)]/[H^+]$ ratio around Titan's orbit (Thomsen et al., 2010), where $(m/q = 2)$ is more likely to be H_2^+. Hence, when solar wind and inner magnetosphere plasma are mixed together, or where the solar wind penetrates the magnetosphere, we might find a depressed relative counts ratio compared to that found in the inner magnetosphere ($He^{++}/H^+ < H_2^+/H^+$).

3.1. Survey

We collected the data of the TOF instrument on CAPS/IMS from 2004 through 2012, and we binned them in three different ways, to look at the data from different points of view:

1. In KSMAG coordinate system we binned the data
   - in 2 R_S × 2 R_S bins in the *X*-*Y* coordinates in the equatorial plane, summing together all the TOF spectra in the *Z* coordinates;
   - 2 R_S × 2 R_S bins in the *Y*-*Z* plane, summing together all the TOF spectra in the *X* coordinate, where we could select whatever numbers of bins in *X* we could sum.
2. In a cylindrical coordinate system, we binned the data in bins measuring 1 R_S× 7.5° (0.5 hr LT) bins, namely, with radial distance as radial coordinate and LT as angular coordinate, in the equatorial plane, summing together all the TOF spectra in the *Z* coordinates; this approach allowed us to explore the data with more resolution and added information to the results obtained with Cartesian binning.
3. We binned the data in a frame with higher resolution in radial distance from the planet versus longitude (0.1 R_S× 20° bins) with respect to the moons Enceladus, Dione, Rhea, and Titan; all the data in the *Z* coordinates were collapsed together. This approach to the data allowed us to look for changes between the upstream and downstream plasma for each moon.

The data processing accounts for a number of instrumental and telemetry mode issues, in order to minimize biases that could have been given by the way data were collected, or packed to be returned to Earth, and also where the spacecraft was located with respect to the magnetosphere. We wanted to make the data as homogeneous as possible to be fitted together or, if that was not possible, fitted separately and then combined as a second step. At this stage, we implemented the following selection:

1. Firstly, since B cycles can last, according to the telemetry mode, either 8, 16, or 32 A cycles, if a change in the data acquisition setting from A cycle to A cycle in the same B cycles occurs, we have to exclude that B cycle from our study. Therefore, our code checks that both sweep table number and microchannel plate voltage stay the same for all the A cycles in a specific B cycle.
2. Since B cycles have different durations, we convert the measured counts/accumulation into counts per second using the B cycle duration for each spectrum.
3. Furthermore, we calculated—through Spacecraft Planet Instrument C-matrix ("Camera matrix") Events (SPICE), the NASA ancillary information system—the distance of the spacecraft from each major moon, in terms of the specific moon radius.
4. Our aim is to study the plasma composition inside the magnetosphere; therefore, we wanted to make sure that all the data we were analyzing were indeed inside the magnetosphere. In order to exclude all data from outside the magnetopause, we obtained a list of magnetopause crossings from N. Pilkington (private communication, 2015), which were used in a study of the magnetopause (Pilkington et al., 2015). Our code, then, runs through the B cycles and classifies them as inside or outside the magnetosphere. Since we do not know what angle the spacecraft trajectory had to the magnetopause during the crossing, we do not know the duration of the crossings; to make sure we keep B cycles from only inside the magnetosphere then, we consider that crossings last for a minimum of 2 hr. Each spectrum was classified into four groups, so that we could select which B cycles we want to process later in the analysis (data inside the magnetosphere,

data outside the magnetosphere, data collected during a magnetosphere crossing, and data that cannot be classified).

The data resulting by this part of the analysis were then fitted as explained in the next section.

3.2. Fitting

As mentioned in the previous section, after the data reduction, the TOF spectra (E/q, TOF channel) for each bin are then summed together and fitted with the code provided from Dan Reisenfeld (private communication 2013). This fitting procedure uses calibration functions for CAPS/IMS and had already been used in previous studies (e.g., Thomsen et al., 2010). The model function used for fitting is a linear combination of the basis functions, H^+, H_2^+, or He^{++} (representing $m/q = 2$), C^+, N^+, O^+, OH^+, H_2O^+, and H_3O^+, which also considers the contribution of heavier molecules that break into daughter species and the background basis function that consists of a straight line. The function returns counts for each species and the error associated to the counts. The function is then minimized with the Levenberg-Marquardt technique.

Further filtering on the data was performed at this stage as well:

1. From SOI up until 2005 doy 058 hr 01:00:00 (2005-058T01:00), the 512 channels corresponded to every fourth channel of the full 2048, for both ST and linear electric field. However, after a few months of TOF data from Saturn, it was understood that many of the TOF channels were never populated by counts. As a consequence, after 2005-058T01:00, the returned 512 channels correspond to a start channel that equals to 40, with every other channel returned up to channel 1062. We, therefore, performed the fits on the two cases separately, and the results were combined later on and the errors were propagated accordingly (see next section).
2. In order to avoid having possible biases in LT variability (due to possible multiple moon encounters in a specific sector of the magnetosphere), we excluded from the analysis B cycles collected when the spacecraft was closer to each major moon (Titan, Rhea, Enceladus, Tethys, Dione, Iapetus, and Hyperion) than 10 moon radii.
3. We only fit for energy steps from 3 to 31 (see Wilson et al., 2012, available at http://ppi.pds.nasa.gov/), $E/q \simeq 1.19-21{,}300$ eV/q.
4. We do not consider heavier species in the fit (e.g., O_2^+, N_2^+, NH^+, NH_2^+, and NH_3^+).

The model returns the counts associated with each species under consideration, as a function of E/q. We start by assuming that the spectrum contains H^+, $m/q = 2$, O^+, OH^+, H_2O^+, and H_3O^+ and fits the model to the summed spectrum. The counts are divided by the efficiencies, which are energy and species dependent: The counts of a certain species at a certain energy are divided by the efficiency of that species at that energy. Then, the counts for each species are integrated in E/q, and if one species is consistent with 0 count within error, that species is removed from the fit and the fit is recalculated with the remaining species. This is continued until no more species are discarded. After that, lastly, the counts are integrated in E/q to get the total counts for each species.

3.3. Analysis and Plotting

Before plotting, we analyze the results of the fits. As mentioned in section 3.2, we fitted separately the two most common options of returning 512 channels: from 0 to 2048 taking every fourth channel (filter 1) and from channels 40 to 1062 returning every other channel (filter 2). Hence, at this stage, we combine the results for the two filters, calculate the ratios, and calculate the errors propagating the uncertainties from the fit on the various species and on the ratios between species. Effectively, with ratio of counts we indicate the ratio of corrected count rates.

In Figure 2 we report a schematic to illustrate the data processing, from the TOF data to the ratios. The schematic shows, as an example for the binning step, the case in which the bins are in XY in KSMAG coordinates.

In Figure 3 we show the results of the fitting, performed on original data and reduced data: In the plot on the left we show the results for $[(m/q = 2)]/[H^+]$ only from the fitting, before all the data reduction and analysis steps were implemented, and in the plot on the right we show the data left after the data reduction was performed. In Figure 3, right, we represented with gray-colored bins, spatial bins where the spacecraft had passed, but we have data with relative error larger than 50% or where the data were reduced.

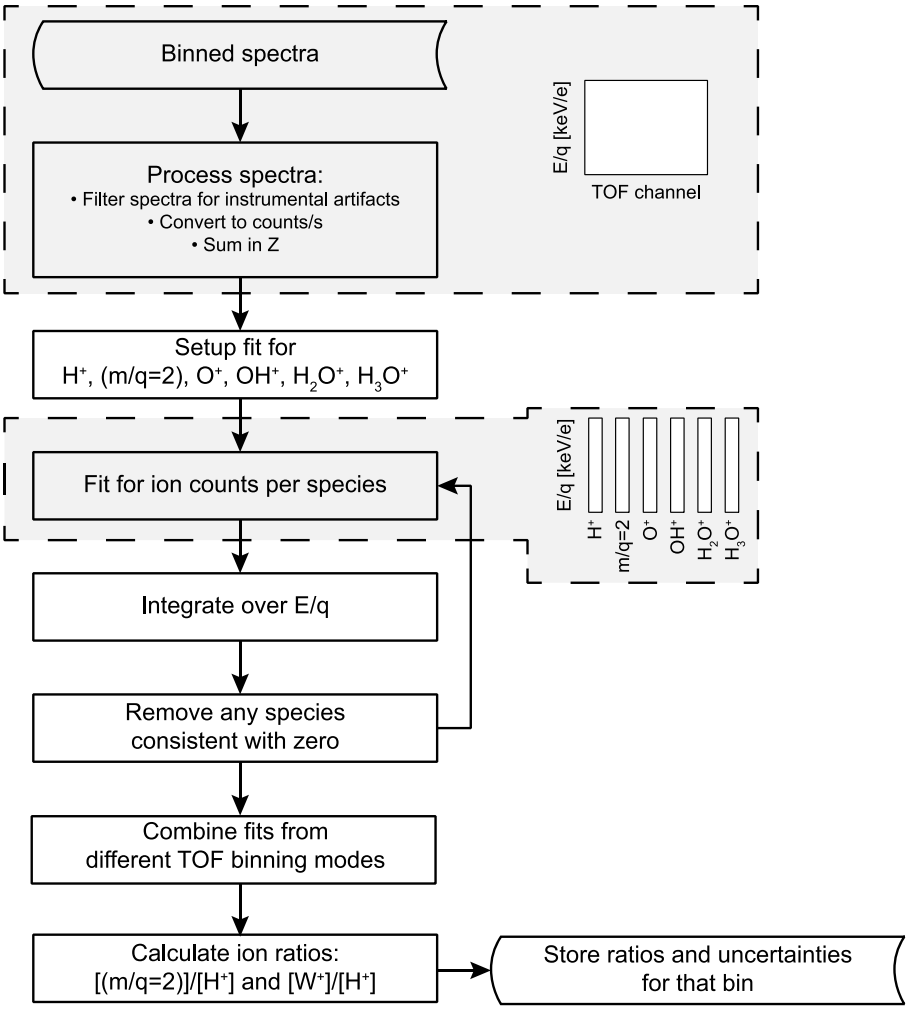

Figure 2. Schematic of the data processing, and as an example for the binning step, the case in which the bins are in *XY* in KSMAG coordinates.

4. Abundance of He^{++} or H_2^+ to Protons: $[(m/q = 2)]/[H^+]$

In Figure 4, a zoom in of Figure 3, right, we show the ratio $[(m/q = 2)]/[H^+]$ in the equatorial *X*-*Y* plane in the KSMAG coordinate system. We plot the maximum and minimum position of the magnetopause calculated by Arridge et al. (2006) to represent the magnetopause positions at extremes of the solar wind conditions and the orbit of Enceladus (circle at 4 R_S) and of Titan (circle at 20 R_S).

We know that TOF does not discriminate between species with the same m/q; therefore from TOF data we cannot differentiate between H_2^+, from inside the magnetosphere, and He^{++} from the solar wind. However, the relative density $[He^{++}]/[H^+]$ peaks at ≃4% but can reach ≃7–8%, in the solar wind (Kasper et al., 2007; Wang, 2008) and from Blanc et al. (2015, and references therein) we know that at higher energies the relative density $[H_2^+]/[H^+] \simeq 0.17$, whereas $[H^{++}]/[H^+] \simeq 0.0029$ in the inner magnetosphere. In addition, we expect a high relative density $[(m/q = 2)]/[H^+]$ around Titan's orbit (Thomsen et al., 2010), where $(m/q = 2)$ is more likely to be H_2^+. Hence, when solar wind and inner magnetosphere plasma mix, or where the solar wind penetrates the magnetosphere, we might find a depressed ratio compared to that found in the inner magnetosphere ($[He^{++}]/[H^+] < [H_2^+]/[H^+]$).

For distances from the planet between 2 and 6 R_S the $[(m/q = 2)]/[H^+]$ ratio ranges between 0.01 and about 0.08. We find a value of the ratio larger in the dusk sector compared to dawn.

From 6 R_S to 10 R_S the ratio varies from ≃0.09 to 0.4. In the afternoon (1200–1800 LT) and premidnight (1800–0000 LT) sectors, from ≃10 R_S (Rhea's orbital distance = 8.7 R_S) outward, the ratio starts increasing

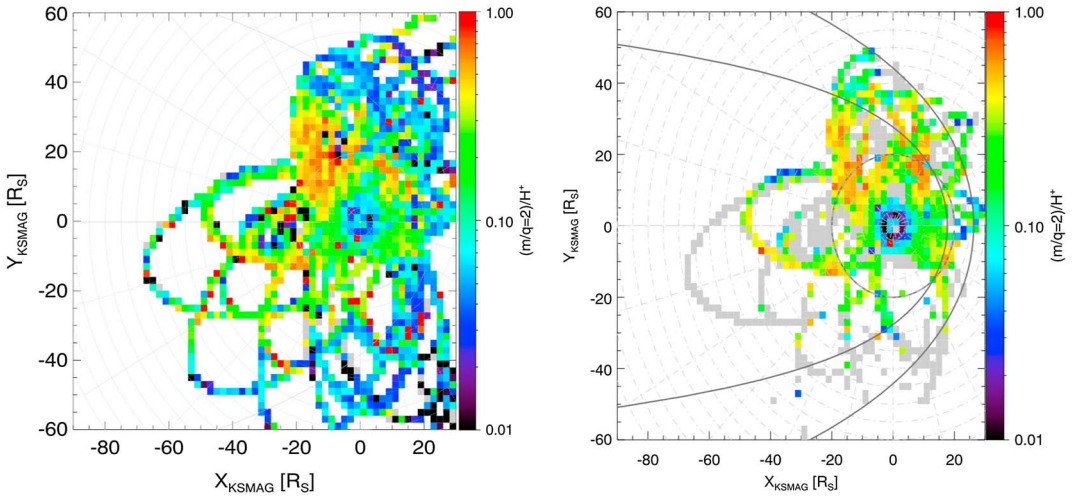

Figure 3. Ratio $[(m/q = 2)]/[H^+]$ before the data reduction (left) and after the data reduction (right). We reported data binned in 2 $R_S \times 2\,R_S$ bins in the equatorial plane (X-Y in KSMAG coordinate system). Columns in Z with a 2 $R_S \times 2\,R_S$ base in the equatorial X-Y plane are collapsed together in the same bin in X-Y. Saturn is located at the origin, dayside is on the positive X direction on the right, in the positive Y direction we find the dusk sector, midnight is on the left, and dawn sector is at the bottom of the plot. In the plots, we reported, as gray curves, the average position of the magnetopause (on the plot on the left) and maximum and minimum positions of the magnetopause (on the plot on the right in dark gray) with parameters estimated by Arridge et al. 2006 to represent the magnetopause positions in both extremes of the solar wind conditions and gray circles representing Enceladus' orbit (4 R_S) and Titan's orbit (20 R_S). We excluded from the plot on the right data with relative error larger than 50% so that the analysis was not biased by TOF spectra with poor signal to noise: In gray we plotted bins where the spacecraft had passed, but data were excluded either as a result of the data reduction process or due to the large relative error.

approaching ≃0.6–0.7, reaching the farthest distance from the planet at ≃40 R_S, at ≃1830–1900 LT. We expected an increase in the ratio around 8–9 R_S, due to Rhea, and 20 R_S, due to Titan (Thomsen et al., 2010; Tseng et al., 2011), as these are both sources of H_2^+. We cannot know if this high ratio region we see at dusk extends at farther distances and later LT, although beyond 27 R_S downtail we find a much smaller ratio (≃0.2–0.3), suggesting that the high ratio region is coming to an end.

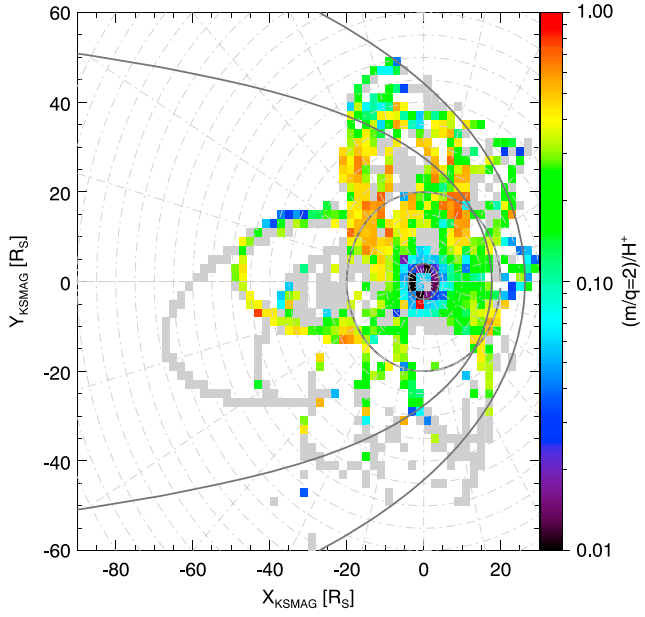

Figure 4. Ratio $[(m/q = 2)]/[H^+]$. Figure format is the same as in Figure 3, right.

Even though the coverage at dawn is more sparse than the coverage at dusk, we can still notice that the ratio at dawn is lower than the ratio at dusk. This suggests that heavier ions ($m/q = 2$) got lost either downtail via plasmoids, or along the magnetopause flanks.

It has to be kept in mind that we are dealing with a ratio between two species so, if one of the two changes, the ratio changes. Hence, a decrease in the ratio may be produced by an increase in H^+, not a decrease in $m/q = 2$. Future studies are needed to shed light on this subject.

In addition to seeing a lower ratio at dawn, we see bins that show a ratio that might result from a combination between the two $m/q = 2$ species, along the magnetopause ($[m/q = 2]/[H^+] \simeq 4\%$), and very clearly around the magnetopause subsolar point.

Three investigations were carried out to examine if the extensions of the high ratio region in the dusk sector were related to biases introduced by (a) averaging very different abundances in the vertical plane, (b) magnetospheric tilt, and (c) type of binning and proximity to moons.

4.1. $[(m/q = 2)]/[H^+]$: Y-Z in KSMAG

We examined the distribution of the ratio in the Y-Z plane to verify that the high ratio region that we see at dusk (see Figure 4) is not due to the fact that many vertical bins are collapsed together in the same bin in X-Y. Figure 5 shows, as example, $[(m/q) = 2]/[H^+]$ for $-26\,R_S < X < -14\,R_S$

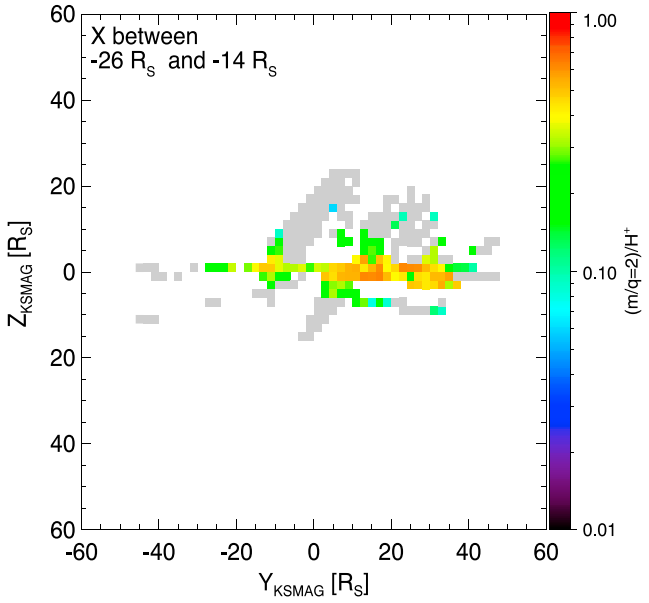

Figure 5. Ratio of counts $[(m/q = 2)]/[H^+]$ in the *Y*-*Z* plane, *X* between −26 R_S and −14 R_S in the tail. Saturn is located in the origin of the axis; on the positive *Y* we have dusk sector; on the negative *Y*, the dawn sector; for positive *Z* we have north hemisphere; and for negative Z, the south hemisphere. We excluded from our plots data with relative error larger than 50% so that the analysis was not biased by time-of-flight spectra with poor signal to noise: In gray we plotted bins where the spacecraft had passed, but data were excluded either as a result of the data reduction process or due to the large relative error. KSMAG = Kronocentric Solar Magnetic.

in the tail. To produce this projection, the data were analyzed as before, but instead of collapsing the bins in *Z* they were integrated over a range in *X* and split into bins in *Z*.

In the dawnside, the ratio reaches a value of ≃0.6, and this value extends from about 10 to 16 R_S far from the planet in the *Y* axis. Even though we do not have much vertical coverage, beyond 15 R_S from the planet, the ratio is lower than what is seen at closer distances, suggesting that, even if we had vertical coverage, we would possibly still have lower ratio. Around 12 R_S, where we have bins showing high ratio, we also have more vertical coverage, and we can see how there the high ratio (≃0.4–0.6) does not extend vertically (4 R_S) as much as it does at dusk (6 R_S). At dusk, the ratio reaches a value ≃0.7, therefore larger than at dawn, extends vertically ≃2 R_S larger than at dawn, and extends for 38 R_S in width. Therefore, the data suggest that the high ratio region that we see in the *X*-*Y* plane at dusk, is about 6 R_S thick and about 38 R_S wide.

At higher latitudes, we see bins that show a value of the ratio lower than 0.1: Since this value of the ratio seems to appear also at dusk on the equatorial plane, at distances from the planet ≃40 R_S, we might be detecting regions with a mixed composition from solar wind and inner magnetosphere. However, we must consider that $m/q = 2$ and H^+ have different scale height (Hill & Michel, 1976), so the vertical extension of the high ratio region does not necessarily reflect the dimensions of the plasma sheet.

4.2. [(m/q=2)]/[H⁺]: Seasonal Variability

Secondly, we wanted to investigate if there were a seasonal difference for the high ratio we see in the dusk sector in Figure 4, and if this had any relation with the magnetospheric tilt with respect to the solar wind. In Figure 6 we show seasonal separation for the data: Figure 6a shows data from the nearer solstice periods—data before 11 February 2008 and after 11 February 2011—and Figure 6b shows data from near the equinox, after 11 February 2008 and before 11 February 2011. During solstices, the absolute value of the magnetospheric tilt angle ranges from 10° to 25°.

We can see that the high ratio region seen at dusk is present in both plots: Figure 6a shows a high ratio region starting around Rhea's radial distance from the planet and expanding outward at dusk. Data from nearer

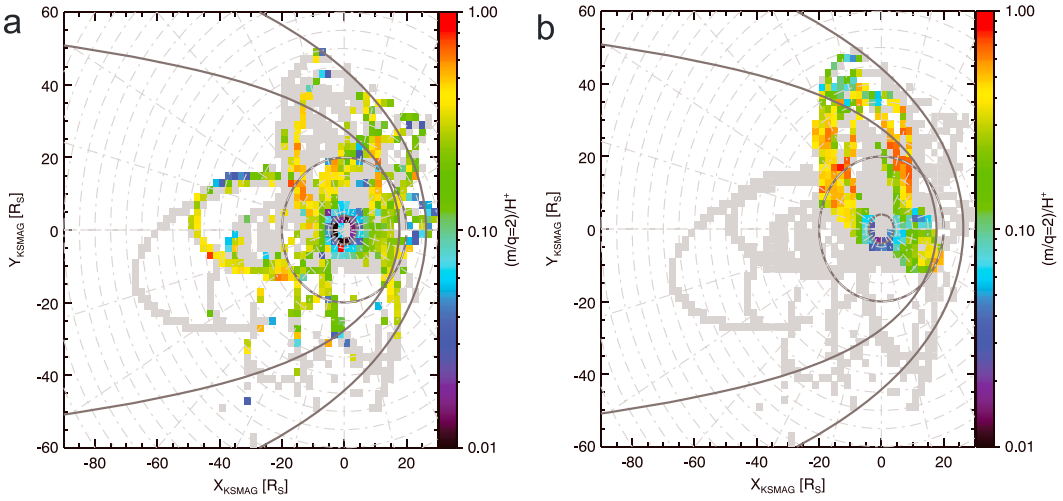

Figure 6. Ratio of counts $[(m/q = 2)]/[H^+]$ for nearer solstice (a), includes data before 11 February 2008 and after 11 February 2011, when the absolute value of the magnetospheric tilt angle ranges from 10° to 25°, and nearer equinox (b) after 11 February 2008 and before 11 February 2011. Figure format is the same as in Figure 4. KSMAG = Kronocentric Solar Magnetic.

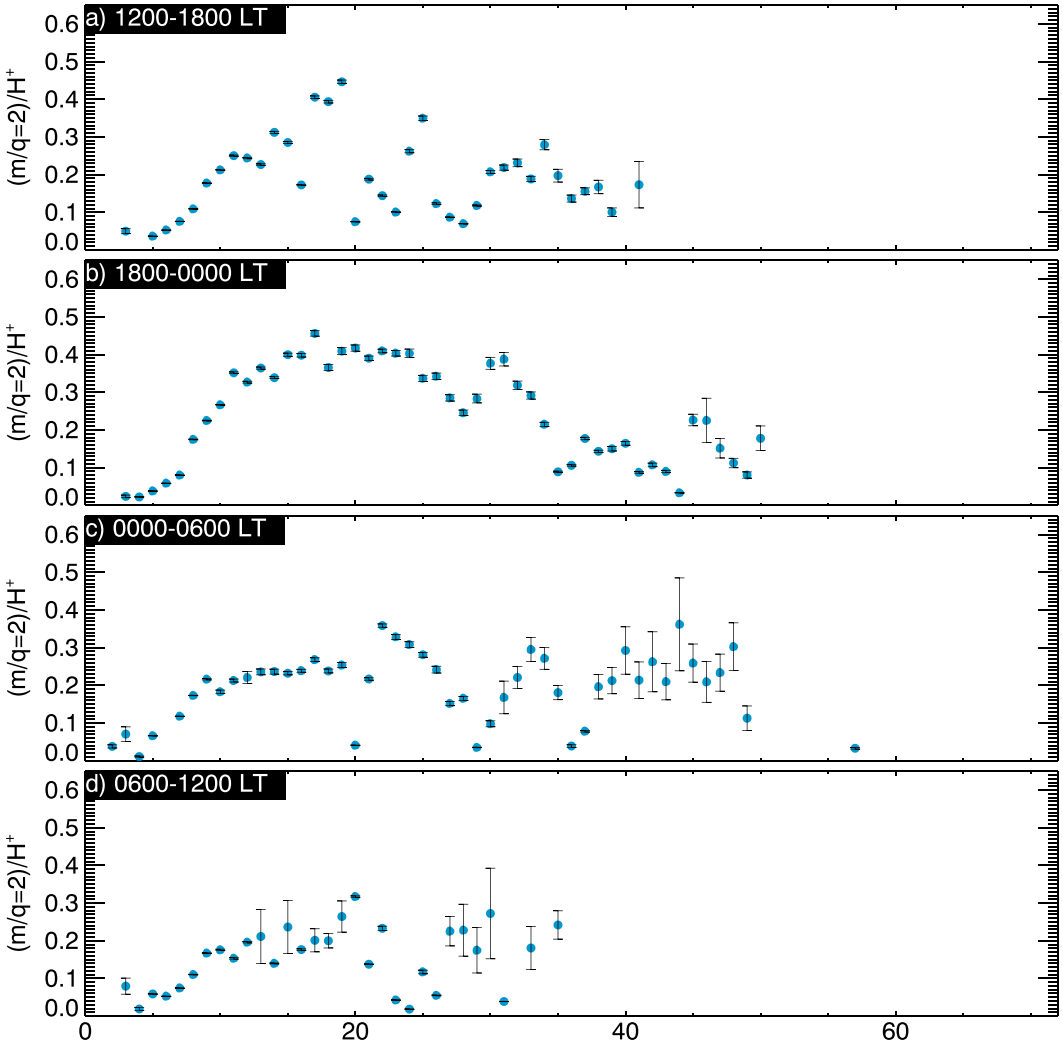

Figure 7. The plot shows the variation of $[(m/q = 2)]/[H^+]$ with distance from Saturn for bins covering 6 hr in LT. In panels a, b, c, and d, respectively, we show sectors from 1200 to 1800 (afternoon), from 1800 to 0000 (premidnight), from 0000 to 0600 (postmidnight), and from 0600 to 1200 LT (prenoon). The time-of-flight spectra in the Z coordinates are summed together, as done for the Kronocentric Solar Magnetic coordinates. We excluded from our plot data with relative error larger than 50% so that the analysis was not biased by time-of-flight spectra with poor signal to noise. LT = local time.

equinox overlap on the high ratio region close to Rhea's orbital distance seen in the data at times closer to solstice and then extends in the dusk sector, as the orbital coverage has changed. Although the spacecraft does not cover completely the dusk high ratio region when nearer to solstices, we see from Figure 6 that the high ratio region we see at dusk, and not at dawn, is not a consequence of the magnetospheric tilt with respect to the solar wind.

4.3. $[(m/q = 2)]/[H^+]$: Radial, Local Time, and Longitudinal Variability

We binned the data in cylindrical coordinates and longitudinal coordinates to understand if the high ratio region present at dusk and seen in Figure 4 was affected by the Cartesian binning or the proximity to the moons. In cylindrical coordinates we binned the data in basic bins that measure 1 $R_S \times 7.5°$ (0.5 hr LT). These bins, can be combined to span a larger LT sector. In Figure 7 each panel represents a 6-hr LT sector from 1200 to 1800 (afternoon), from 1800 to 0000 (premidnight), from 0000 to 0600 (postmidnight), and from 0600 to 1200 LT (prenoon). We show the ratio for 6 hr in LT as a function of distance from Saturn. The errors that we show in the plots are those calculated through error propagation techniques from the errors given by the fit. We can appreciate how, from sector to sector, the high ratio extends to different distances from the planet.

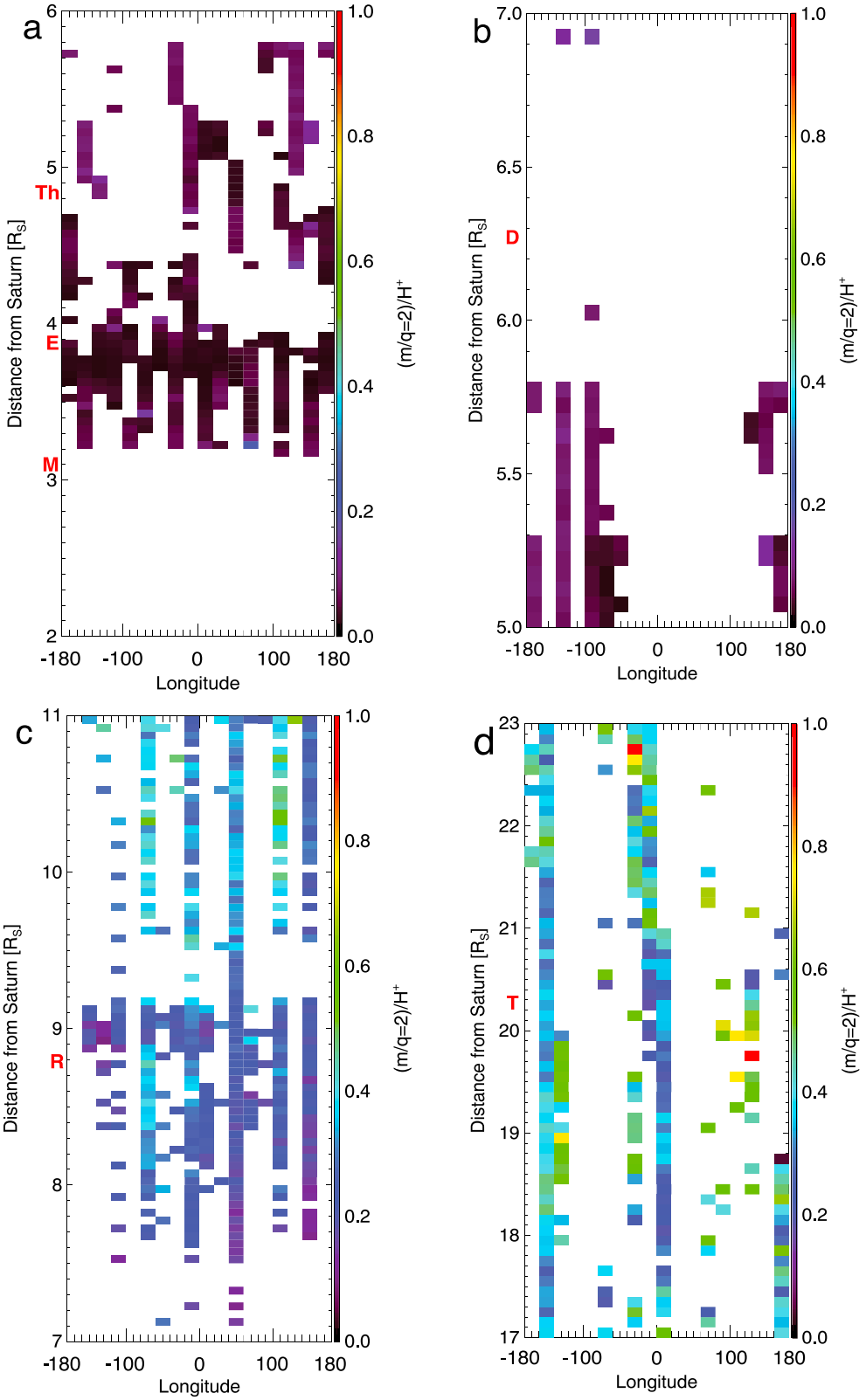

Figure 8. In this plot we show the $[(m/q = 2)]/[H^+]$ as a function of distance from Saturn and the longitude of the spacecraft with respect to Enceladus (panel a), Dione (panel b), Rhea (panel c), and Titan (panel d), in the premidnight sector, namely, from 1800 to 0000 LT. We indicated on the plots also the orbital distance for Mimas (M), Enceladus (E), Tethys (Th), Rhea (R), and Titan (T).

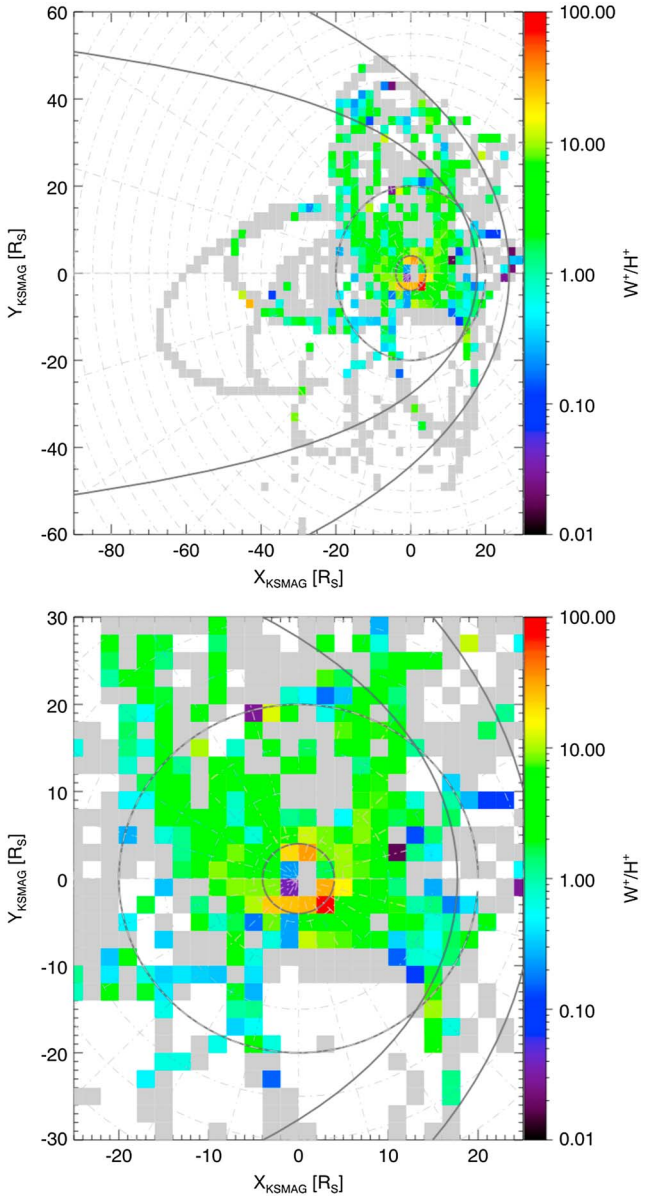

Figure 9. Ratio $[W^+]/[H^+]$. Figure format is the same as in Figure 4 (top) and a zoom in of the inner magnetosphere. Figure format is the same as in Figure 4. KSMAG = Kronocentric Solar Magnetic.

In the afternoon sector (1200–1800 LT), see Figure 7a, the ratio starts increasing at about 5 R_S, and peaks around 19 R_S. After a dip in the ratio around 20 R_S, the ratio has a further peak after 30 R_S. Large errors might indicate that, in the presence of lower counts, the fitting code might have a less accurate performance. In the premidnight sector (1800–0000 LT), see Figure 7b, the ratio begins to increase around 5 R_S and peaks at around 17 R_S. After that radial distance the ratio decreases to lower values, and it peaks again around 30 R_S and 45 R_S; however, a larger error is associated with the latter. In the postmidnight sector (0000–0600 LT), see Figure 7c, the highest ratio is reached at about 22 R_S, and then again beyond 40 R_S, with very large errors associated to these values. The premidnight and postmidnight sectors are the sectors where the ratio drops at a higher distance from the planet, since the plasma from the inner magnetosphere can be transported in the tail. In the prenoon sector (0600–1200 LT), see Figure 7d, the ratio increases until 20 R_S, and peaks again at $\simeq$ 30 R_S.

From Figure 7, we can see that the maximum ratio of $\simeq$0.48 in the afternoon sector drops to a maximum value of $\simeq$0.45 in the premidnight sector, then it drops again to $\simeq$0.4 in the postmidnight sector, to drop to a maximum value of $\simeq$0.3 in the prenoon sector. Through this analysis, we were able to appreciate that the $[(m/q = 2)]/[H^+]$ ratio diminishes progressively as one moves from one sector to another sector beyond $\simeq$10 R_S radial distance from the planet.

Lastly, we wanted to investigate whether the high ratio we see at dusk in Figure 4 is a feature possibly created by a proximity with the moons. Therefore, we looked at the ratio of counts as a function of distance from the planet and longitude of the spacecraft with respect to the moons Enceladus (E; Figure 8a), Dione (D; Figure 8b), Rhea (R; Figure 8c), and Titan (T; Figure 8d), and we report the case for the premidnight sector (1800–0000 LT). In Figure 8a we also report the position of the moons Mimas (M) and Tethys (Th). The bins measure 0.1 R_S in radial distance and 20° in longitude. We start having data coverage beyond Mimas distances (see Figure 8a) where the ratio is <0.2, then the ratio drops around Enceladus' orbit, up to Tethys distances, where it increases slightly, always to stay <0.2. However, when we do have coverage, we can appreciate how the ratio does not seem to be affected by being measured upstream (negative values of longitude) or downstream (positive values of longitude) to a moon. This suggests that the high ratio region that we see at dusk is not an effect given by moon proximity.

5. Abundance of W^+ to Protons: $[W^+]/[H^+]$

In Figure 9 (top) we show the relative counts $[W^+]/[H^+]$ in the *X*-*Y* plane, and in Figure 9 (bottom) a zoom in of the inner magnetosphere for the same ratio. Near the orbit of Enceladus $[W^+]/[H^+] > 10$ can be seen. In the dusk sector at that radial distance, the ratio of counts has lower maximum values ($\simeq$10–20) compared to dawn ($\simeq$20–50), but the high $[W^+]/[H^+]$ ratio is more extended (from 2 to 6 R_S) compared to dawn (from 2 to 4 R_S). We also see some bins with ratio larger than 10 downtail after midnight.

As mentioned before, we binned the data in cylindrical coordinates in basic bins that measure 1 $R_S \times 7.5°$ (0.5 hr LT). These bins, can be combined to span a larger LT sector. In Figures 10a and 10b we show the relative counts $[W^+]/[H^+]$ as a function of distance from Saturn, for two 12-hr bins, respectively from 1200 to 0000 (dusk) and from 0000 to 1200 (dawn). The errors that we show in the plots are those calculated through error propagation techniques from the errors given by the fit. We can appreciate how we have lower maximum values of the $[W^+]/[H^+]$ ratio at dusk but with the higher ratio region more spread in radial distance from the planet, opposite to that we find at dawn, where we have higher values of the ratio but with a sharper

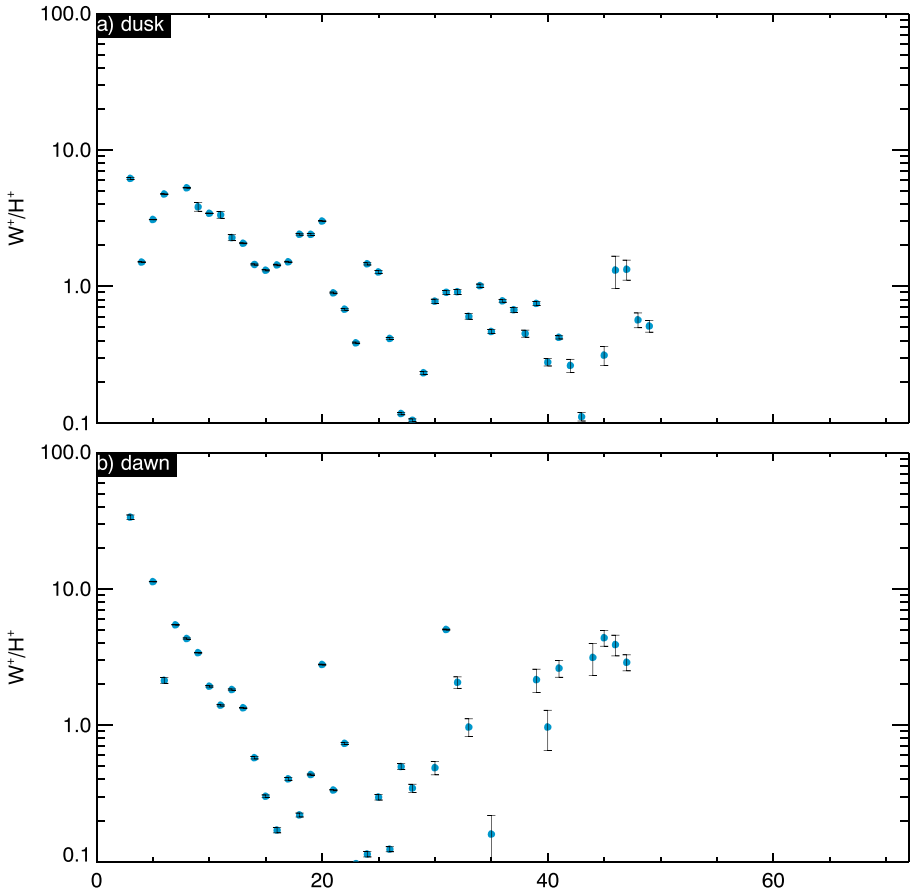

Figure 10. The plot shows the variation of $[W^+]/[H^+]$ with distance from Saturn for bins covering 12 hr in LT. Panels a and b show respectively sectors from 1200 to 0000 (dusk) and from 0000 to 1200 (dawn). The time-of-flight spectra in the *Z* coordinates are summed together, as done for the Kronocentric Solar Magnetic coordinates. We excluded from our plot data with relative error larger than 50% so that the analysis was not biased by time-of-flight spectra with poor signal to noise.

drop before reaching 10 R_R. We also find that $[W^+]/[H^+]$ increases again at higher distances from the planet (around 35 R_S in the dusk sector and around 40 R_S at dawn).

6. Discussion

We presented a survey that used data from IMS/TOF on Cassini/CAPS from 2004 through to 2012. After a complex data reduction we fitted the TOF distribution with a code that uses TOF calibration functions for CAPS/IMS. We obtained relative counts $[(m/q = 2)]/[H^+]$ and $[W^+]/[H^+]$. We reported data binned in KSMAG coordinate system, through 2 $R_S \times 2\,R_S$ bins in the equatorial plane (*X*-*Y* plane, collapsing together columns of data in *Z* coordinates) and in the *Y*-*Z* plane (collapsing together a chosen range in *X* coordinates). We have used the same data reduction techniques but enhanced the resolution to explore the data studying the relative counts $[(m/q = 2)]/[H^+]$ and $[W^+]/[H^+]$ as a function of LT and radial distance from the planet for a selected portion of LT and also the $[(m/q = 2)]/[H^+]$ ratio as a function of the distance from the planet around four moons (Enceladus, Dione, Rhea, and Titan) and longitude of the spacecraft with respect to each of those moons.

For the $[(m/q = 2)]/[H^+]$ ratio of counts (see Figure 4), we found a very low value in the inner magnetosphere, increasing to approximately 0.1–0.7 in the outer magnetosphere, with trend compatible with that found by Thomsen et al. (2010). Blanc et al. (2015) estimate that the $(m/q = 2)$ at CHEMS energies was ≃84% coming from internal sources and ≃16 % from the solar wind, so it must be considered that plasma detected in the magnetosphere might also have a solar wind component. The ratio was found to increase near Rhea and Titan, which might be a consequence of these satellites being sources of H_2^+ (Tseng et al., 2011).

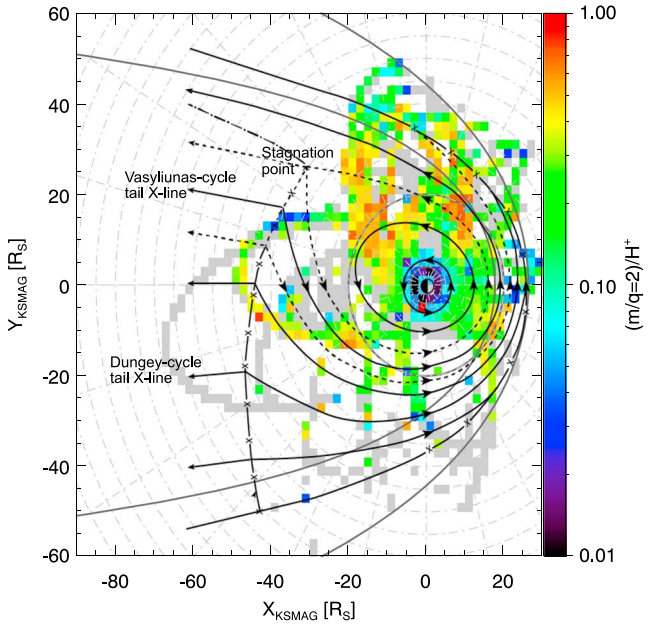

Figure 11. We overlapped Figure 2 from Cowley et al. 2004 to our results shown in Figure 4. We indicated on the plot that solid lines joined by *X*s indicated reconnection line associated with the Dungey cycle and the dashed lines with *X*s reconnection line for the Vasyliunas cycle; we also indicated the location of the stagnation point.

An alternative interpretation for why the ratio starts increasing around Rhea's radial distance might be that the majority of the molecules produced by Enceladus are ionized far away from the moon (Fleshman et al., 2010). In the dusk sector we found a region extending from near the orbit of Rhea to approximately 40 R_S far from the planet, where the ratio was higher than in other LT sectors. The relative density presented by Thomsen et al. (2010) was as a function of radial distance, and so this new survey suggests that at least some of the variability observed by Thomsen et al. (2010) is due to LT variations. We investigated the high $[(m/q = 2)]/[H^+]$ ratio region that we see at dusk in Figure 4 in different ways, and we concluded that it is not due to the fact that we had collapsed bins in *Z* in the same binning in *X*-*Y* (see Figure 5), to season (see Figure 6), to type of binning (see Figure 7), nor to longitude of the spacecraft with respect to the moons (see Figure 8). We concluded that the high $[(m/q = 2)]/[H^+]$ ratio region seen at dusk in Figure 4 is a real LT asymmetry.

We also report the distribution of the $[(m/q = 2)]/[H^+]$ ratio in the *Y*-*Z* plane for $-26\ R_S < X < -14\ R_S$ in the tail; see Figure 5. To produce this projection, the data were analyzed as for the *X*-*Y* plane, but instead of collapsing the bins in *Z* they were integrated over a range in *X* and split into bins in *Z*. We find that the high ratio region that we see in the *X*-*Y* plane at dusk, is about 6 R_S thick and about 38 R_S wide, for this range in *X* coordinates. The fact that we see the high ratio region extending vertically at dusk more than at dawn could be explained with the mechanism modeled by Jia and Kivelson 2016. However, we must consider that $[(m/q = 2)]/[H^+]$ is a ratio between two different species with two different scale heights, therefore the high ratio region that we see does not necessarily represent the effective vertical extension of the plasma sheet.

The high $[(m/q = 2)]/[H^+]$ ratio extends radially to different distances from the planet depending on which of the four LT sectors we are looking (see Figure 7): On average, the maximum ratio ≃0.48 in the afternoon sector, drops to a maximum value ≃0.45 in the premidnight sector, to a maximum value of ≃0.4 in the postmidnight sector, and to a maximum value of ≃0.3 in the prenoon sector. The ratio at prenoon is more than 18% lower than the ratio in the afternoon suggesting that the internally produced plasma has been lost through magnetopause flanks and downtail (Hill et al., 2008; McComas et al., 2017) and/or that the H_2^+ dissociates. McAndrews et al. (2009) and Thomsen et al. (2010) both find that, in the premidnight to dawn sector, beyond 20 R_S, the flow had typically a tailward and dawnward direction; Cowley et al. (2004) and Jia et al. (2012) suggest that plasma is lost along the magnetopause flanks. Thomsen 2013 and Thomsen et al. (2014) find a mass outflow beyond 30 R_S in the dusk sector parallel to the magnetopause, consistent with that modeled by Delamere et al. (2013) and Jia et al. (2012), a dusk wing given either by viscous momentum transfer with the solar wind or by the fact that the inertia of the plasma rotating from the dayside is larger than the planetary magnetic field stress. Future studies are needed to shed light on this subject.

In Figure 11 we overlap the flow pattern suggested by Cowley et al. (2004) onto the map of the $[(m/q = 2)]/[H^+]$ ratio presented in Figure 4. The flow pattern diagram was scaled to match the corotating pattern near Enceladus and the position of the subsolar magnetopause. The flanks of the magnetopause in the flow pattern diagram lie between the minimum and maximum positions of the magnetopause as modeled by Arridge et al. (2006). From this simple scaling we can see that Cassini's orbits have not covered the region in the direction, which the model suggests as location of the stagnation point. However, $[(m/q = 2)]/[H^+]$ is found to fall to < 0.1 around 40 R_S at earlier LTs than the modeled stagnation point. This suggests loss of internally produced plasma down the magnetotail to the solar wind and that the high ratio region coming to an end might actually indicate the end of a plasmasphere. Therefore, these data suggest that the stagnation point is actually at earlier LTs, around 1900 LT, perhaps by a rotation of streamlines in the sketch of Cowley et al. (2004). It is difficult to make a strong statement on the region of the magnetosphere downstream of the Dungey cycle X line on the dawn flank as the coverage is sparse and many of the bins have a high uncertainty.

One anomaly seen in Figure 4 is the depression of $[(m/q=2)]/[H^+]$ between the orbits of Titan and Rhea and an enhancement outside of the orbit of Titan both after 0000 LT. Possible causes that might be working together are chemical reactions with injected energetic protons (Paranicas et al., 2012) charge-exchanging with neutral gas and increasing the H^+ density, thus reducing the $[(m/q = 2)]/[H^+]$ ratio or electron impact-driven chemistry with hot electrons on the nightside (Arridge, private communication, 2015). However, we do not have any directional information, and, therefore, any consideration about this is speculative. Hence, further work is needed in this matter.

Another interesting feature is that we find bins showing high $[(m/q = 2)]/[H^+]$ ratios far from the planet in the dusk sector (see Figure 4), where at lower radial distances we detected lower ratios. Motion of the plasma flow pattern due to expansion/contraction of the magnetosphere could produce such features. We see bins that show a $[(m/q = 2)]/[H^+]$ ratio that might result from a combination between the two $m/q = 2$ species, along the magnetopause, and very clearly around the magnetopause subsolar point. Being a statistical study, we know that during the 9 years represented in our data set, the position of the magnetopause must have varied as a consequence of changes in solar activity; therefore, we do not know, a priori, how far Cassini was from the magnetopause when a particular spectrum was measured, and, in case of Kelvin-Helmholtz instabilities, we cannot estimate how far from the magnetopause the solar wind would have penetrated the magnetosphere or we could be detecting the area outside a plasmasphere.

We find a high relative counts $[W^+]/[H^+]$ around Enceladus (see Figure 9), as expected observationally (Thomsen et al., 2010) and theoretically (Fleshman et al., 2010; Persoon et al., 2009). The fact that the relative abundance of W^+ to H^+ is still high for distances $<3.9\ R_S$ might be due to several factors that could also operate together: (1) the spreading of the Enceladus' neutral cloud (Cassidy & Johnson, 2010), resulting in neutrals transported closer to the planet that then get ionized, (2) Mimas (orbit at $\simeq 3.07\ R_S$), and the rings can be minor plasma sources (Tseng et al., 2013), which is hard to determine since the E ring and Enceladus, and G ring and Mimas could overlap spatially. Sittler et al. (2008) model that the peak of the ion density is located between Tethys and Dione, and Holmberg et al. (2017) measured the ion density peak to be at $4.6\ R_S$ from Saturn, so the fact the we see a high $[W^+]/[H^+]$ ratio around Enceladus and even at lower radial distances from the planet might suggest that although around Enceladus the ion density is low, the majority of the ions is formed by W^+.

Comparing the dusk sector with the dawn sector (see Figure 10) we find that $[W^+]/[H^+]$ maximum values are generally smaller and more radially spread out in the dusk sector. This radial extension asymmetry is found by Holmberg et al. (2014), who find that the ion density is more spread out in the dusk sector compared to the down sector. We also find that $[W^+]/[H^+]$ increases again at higher distances from the planet (around 35 R_S and 47 R_S in the dusk sector and around 20, 35, and 45 R_S at dawn). This may be due to higher abundance of water group ions present in plasmoids: Hill et al. (2008) find that the two plasmoids for which they can determine composition were dominated by water group ions.

We saw differences in LT for both ratios $[(m/q = 2)]/[H^+]$ and $[W^+]/[H^+]$ between dawn and dusk sectors, suggesting a difference in the chemistry and/or the transport between the two sectors, possibly due to convection (Cowley et al., 2004; Jia et al., 2012), noon-to-midnight electric field (Andriopoulou et al., 2012, 2014; Wilson et al., 2013), or presence of hot protons (Paranicas et al., 2012) and electrons (Arridge, private communication, 2015) around midnight at Rhea's distances.

Unfortunately, since directional information is not available for the IMS TOF data it is impossible to determine the direction in which the plasma is flowing. Therefore, we cannot make a definitive statement, for instance, about the position of the X line from these data, although Smith et al. (2016) suggest that the X line should lie around 30 R_S, some of the TOF spectra should have been taken from both sides of the X line. However, these results do provide evidence for circulation and LT asymmetries in Saturn's magnetosphere.

7. Conclusions

Our aim was to have a global picture of plasma flow patterns, to investigate sinks and source mechanisms. The baseline for this study was an extensive analysis and reduction of data from the TOF instrument on CAPS/IMS, from 2004 through 2012, accounting for instrument artifacts, and minimizing instrumental and observational biases, and nonlinear fitting of the TOF spectra.

This is the most comprehensive study ever made of relative abundances of thermal plasma at Saturn, since it utilizes CAPS/IMS data from 2004 through to 2012, which is all the CAPS data from the mission, maximizing the use of Cassini's orbital coverage at Saturn's magnetosphere during those years.

Since this study covers about 9 years of data, we have to consider that in 9 years the magnetosphere changed quite significantly, through solstices and equinox, but also in response to changes in the solar wind conditions, for example, the size of the magnetosphere, its tilt with respect to the solar wind, the activity of the ionosphere as a source of plasma, and the reconnection rate. These seasonal changes could have affected the location of plasma populations and the ratios we are studying. Therefore, for some of the features detected, it is not possible to categorically assert whether they are permanent or isolated due to changing Cassini orbital coverage with time.

In conclusion, we found the plasma composition in Saturn's magnetosphere presents significant LT asymmetries and variability that should be included in models of the system. Some evidence of displacement of the stagnation point toward earlier LTs (≃1900 LT) compared to Cowley et al.'s (2004) plasma circulation model suggests that the solar wind has greater influence on Saturn's magnetosphere than previously predicted.

Future modeling of the features identified, both from the point of view of the chemistry and in terms of magnetospheric circulation, will be crucial to shed light on their origin. Many questions arise from the results of this study. For example, $[(m/q = 2)]/[H^+]$ appears to increase in the outer magnetosphere beyond ≃35 R_S. Is this due to Cassini detecting plasmoids, or is this a permanent characteristic of the system? Why do we see a lower $[(m/q = 2)]/[H^+]$ ratio close to Rhea's orbit around midnight? Moreover, further experimental investigation can be done, for instance studying the $[(m/q = 2)]/[H^+]$, $[W^+]/[H^+]$, and $[O^+, OH^+, H_2O^+, H_3O^+]/[W^+]$ ratio variations during times of different solar activity, and the $[O^+, OH^+, H_2O^+, H_3O^+]/[W^+]$ ratios could be studied as a function of L shell and LT or in Cartesian and cylindrical coordinate system centered on Enceladus.

Acknowledgments
The CAPS/IMS TOF data set is from volume CO-E/J/S/SW-CAPS-2-UNCALIBRATED-V1.0 of the Planetary Data System (PDS) at http://pds.nasa.gov/. M. F. worked on this study while a visiting student at Lancaster University and would like to thank the Department of Physics, staff, and students, for their kindness and support, and in particular James Wild, Sarah Badman, Nathan Case, and Carley Martin. M. F. would like to thank Geraint Jones, Tom Stallard, and Licia Ray for their comments and Jamie Jasinski and Tom Nordheim for their help and support.

References

André, N., Dougherty, M. K., Russell, C. T., Leisner, J. S., & Khurana, K. K. (2005). Dynamics of the Saturnian inner magnetosphere: First inferences from the Cassini magnetometers about small-scale plasma transport in the magnetosphere. *Geophysical Research Letters*, *32*, L14S06. https://doi.org/10.1029/2005GL022643

André, N., Persoon, A. M., Goldstein, J., Burch, J. L., Louarn, P., Lewis, G. R., et al. (2007). Magnetic signatures of plasma-depleted flux tubes in the Saturnian inner magnetosphere. *Geophysical Research Letters*, *34*, L14108. https://doi.org/10.1029/2007GL030374

Andriopoulou, M., Roussos, E., Krupp, N., Paranicas, C., Thomsen, M., Krimigis, S., et al. (2012). A noon-to-midnight electric field and nightside dynamics in Saturn's inner magnetosphere, using microsignature observations. *Icarus*, *220*(2), 503–513. https://doi.org/10.1016/j.icarus.2012.05.010

Andriopoulou, M., Roussos, E., Krupp, N., Paranicas, C., Thomsen, M., Krimigis, S., et al. (2014). Spatial and temporal dependence of the convective electric field in Saturn's inner magnetosphere. *Icarus*, *229*, 57–70. https://doi.org/10.1016/j.icarus.2013.10.028

Arridge, C. S., Achilleos, N., Dougherty, M. K., Khurana, K. K., & Russell, C. T. (2006). Modeling the size and shape of Saturn's magnetopause with variable dynamic pressure. *Journal of Geophysical Research*, *111*, A11227. https://doi.org/10.1029/2005JA011574

Arridge, C. S., Khurana, K. K., Russell, C. T., Southwood, D. J., Achilleos, N., Dougherty, M. K., et al. (2008). Warping of Saturn's magnetospheric and magnetotail current sheets. *Journal of Geophysical Research*, *113*, A08217. https://doi.org/10.1029/2007JA012963

Badman, S. V., & Cowley, S. W. H. (2007). Significance of Dungey-cycle flows in Jupiter's and Saturn's magnetospheres, and their identification on closed equatorial field lines. *Annales Geophysicae*, *25*(4), 941–951. https://doi.org/10.5194/angeo-25-941-2007

Bagenal, F., & Delamere, P. A. (2011). Flow of mass and energy in the magnetospheres of Jupiter and Saturn. *Journal of Geophysical Research*, *116*, A05209. https://doi.org/10.1029/2010JA016294

Blanc, M., Andrews, D. J., Coates, A. J., Hamilton, D. C., Jackman, C. M., Jia, X., et al. (2015). Saturn plasma sources and associated transport processes. *Space Science Reviews*, *192*(1), 237–283. https://doi.org/10.1007/s11214-015-0172-9

Bouhram, M., Johnson, R. E., Berthelier, J. J., Illiano, J. M., Tokar, R. L., Young, D. T., & Crary, F. J. (2006). A test-particle model of the atmosphere/ionosphere system of Saturn's main rings. *Geophysical Research Letters*, *33*, L05106. https://doi.org/10.1029/2005GL025011

Cassidy, T., & Johnson, R. (2010). Collisional spreading of Enceladus' neutral cloud. *Icarus*, *209*(2), 696–703. https://doi.org/10.1016/j.icarus.2010.04.010

Coates, A. J., Wellbrock, A., Lewis, G. R., Arridge, C. S., Crary, F. J., Young, D. T., et al. (2012). Cassini in Titan's tail: CAPS observations of plasma escape. *Journal of Geophysical Research*, *117*, A05324. https://doi.org/10.1029/2012JA017595

Cowley, S. W. H., Bunce, E. J., & Prangé, R. (2004). Saturn's polar ionospheric flows and their relation to the main auroral oval. *Annales Geophysicae*, *22*(4), 1379–1394. https://doi.org/10.5194/angeo-22-1379-2004

Cowley, S. W. H., Nichols, J. D., & Jackman, C. M. (2015). Down-tail mass loss by plasmoids in Jupiter's and Saturn's magnetospheres. *Journal of Geophysical Research: Space Physics*, *120*, 6347–6356. https://doi.org/10.1002/2015JA021500

Crary, F. J., Clarke, J. T., Dougherty, M. K., Hanlon, P. G., Hansen, K. C., Steinberg, J. T., et al. (2005). Solar wind dynamic pressure and electric field as the main factors controlling Saturn's aurorae. *Nature*, *433*(7027), 720–722.

Delamere, P. A., & Bagenal, F. (2010). Solar wind interaction with Jupiter's magnetosphere. *Journal of Geophysical Research*, *115*, A10201. https://doi.org/10.1029/2010JA015347

Delamere, P. A., Wilson, R. J., Eriksson, S., & Bagenal, F. (2013). Magnetic signatures of Kelvin-Helmholtz vortices on Saturn's magnetopause: Global survey. *Journal of Geophysical Research: Space Physics*, *118*, 393–404. https://doi.org/10.1029/2012JA018197

DiFabio, R. D. (2012). Spatial and temporal variations of the suprathermal (3-220 keV/e) ion composition in Saturn's equatorial magnetosphere (PhD Thesis). College Park, MD.

DiFabio, R. D., Hamilton, D. C., Krimigis, S. M., & Mitchell, D. G. (2011). Long term time variations of the suprathermal ions in Saturn's magnetosphere. *Geophysical Research Letters*, *38*, L18103. https://doi.org/10.1029/2011GL048841
Dungey, J. W. (1961). Interplanetary magnetic field and the auroral zones. *Physical Review Letters*, *6*(2), 47–48.
Elrod, M. K., Tseng, W. L., Wilson, R. J., & Johnson, R. E. (2012). Seasonal variations in Saturn's plasma between the main rings and Enceladus. *Journal of Geophysical Research*, *117*, A03207. https://doi.org/10.1029/2011JA017332
Felici, M., Arridge, C. S., Coates, A. J., Badman, S. V., Dougherty, M. K., Jackman, C. M., et al. (2016). Cassini observations of ionospheric plasma in Saturn's magnetotail lobes. *Journal of Geophysical Research: Space Physics*, *121*, 338–357. https://doi.org/10.1002/2015JA021648
Fleshman, B. L., Delamere, P. A., & Bagenal, F. (2010). A sensitivity study of the Enceladus torus. *Journal of Geophysical Research*, *115*, E04007. https://doi.org/10.1029/2009JE003372
Fleshman, B. L., Delamere, P. A., Bagenal, F., & Cassidy, T. (2013). A 1-D model of physical chemistry in Saturn's inner magnetosphere. *Journal of Geophysical Research: Planets*, *118*, 1567–1581. https://doi.org/10.1002/jgre.20106
Hansen, C. J., Esposito, L., Stewart, A. I. F., Colwell, J., Hendrix, A., Pryor, W., et al. (2006). Enceladus' water vapor plume. *Science*, *311*(5766), 1422–1425. https://doi.org/10.1126/science.1121254
Hill, T. W. (1979). Rates of mass, momentum, and energy transfer at the magnetopause. In B. Battrick, J. Mort, G. Haerendel, & J. Ortner (Eds.), *Magnetospheric Boundary Layers*. Retrieved from http://adsabs.harvard.edu/abs/1979ESASP.148..325H
Hill, T. W., Dessler, A. J., & Goertz, C. K. (1983). Magnetospheric models. In A. J. Dessler (Ed.), *Physics of the Jovian Magnetosphere* (Cambridge Planetary Science Old) (pp. 353–394). Cambridge:Cambridge University Press. Cambridge Books Online. https://doi.org/10.1017/CBO9780511564574.012
Hill, T. W., & Michel, F. C. (1976). Heavy ions from the Galilean satellites and the centrifugal distortion of the Jovian magnetosphere. *Journal of Geophysical Research*, *81*(25), 4561–4565. https://doi.org/10.1029/JA081i025p04561
Hill, T. W., Rymer, A. M., Burch, J. L., Crary, F. J., Young, D. T., Thomsen, M. F., et al. (2005). Evidence for rotationally driven plasma transport in Saturn's magnetosphere. *Geophysical Research Letters*, *32*, L14S10. https://doi.org/10.1029/2005GL022620
Hill, T. W., Thomsen, M. F., Henderson, M. G., Tokar, R. L., Coates, A. J., McAndrews, H. J., et al. (2008). Plasmoids in Saturn's magnetotail. *Journal of Geophysical Research*, *113*, A01214. https://doi.org/10.1029/2007JA012626
Holmberg, M. K. G., Shebanits, O., Wahlund, J., Morooka, M. W., Vigren, E., André, N., et al. (2017). Density structures, dynamics, and seasonal and solar cycle modulations of Saturn's inner plasma disk. *Journal of Geophysical Research*, *122*, 12,258–12,273. https://doi.org/10.1002/2017JA024311
Holmberg, M., Wahlund, J. E., & Morooka, M. (2014). Dayside/nightside asymmetry of ion densities and velocities in Saturn's inner magnetosphere. *Geophysical Research Letters*, *41*, 3717–3723. https://doi.org/10.1002/2014GL060229
Holmberg, M., Wahlund, J.-E., Morooka, M., & Persoon, A. (2012). Ion densities and velocities in the inner plasma torus of Saturn. *Planetary and Space Science*, *73*(1), 151–160. https://doi.org/10.1016/j.pss.2012.09.016, solar System science before and after Gaia.
Jia, X., Hansen, K. C., Gombosi, T. I., Kivelson, M. G., Tóth, G., DeZeeuw, D. L., & Ridley, A. J. (2012). Magnetospheric configuration and dynamics of Saturn's magnetosphere: A global MHD simulation. *Journal of Geophysical Research*, *117*, A05225. https://doi.org/10.1029/2012JA017575
Jia, X., & Kivelson, M. G. (2016). Dawn-dusk asymmetries in rotating magnetospheres: Lessons from modeling Saturn. *Journal of Geophysical Research: Space Physics*, *121*, 1413–1424. https://doi.org/10.1002/2015JA021950
Johnson, R., Luhmann, J., Tokar, R., Bouhram, M., Berthelier, J., Sittler, E., et al. (2006). Production, ionization and redistribution of O_2 in Saturn's ring atmosphere. *Icarus*, *180*(2), 393–402. https://doi.org/10.1016/j.icarus.2005.08.021
Johnson, R. E., Smith, H. T., Tucker, O. J., Liu, M., Burger, M. H., Sittler, E. C., & Tokar, R. L. (2006). The enceladus and OH tori at Saturn. *The Astrophysical Journal Letters*, *644*, L137–L139. https://doi.org/10.1086/505750
Johnson, R. E., Tucker, O. J., Michael, M., Sittler, E. C., Smith, H. T., Young, D. T., & Waite, J. H. (2010). *Titan From Cassini-Huygens, Mass loss processes in Titan's upper atmosphere* (pp. 373–391). Dordrecht: Springer Netherlands. https://doi.org/10.1007/978-1-4020-9215-2_15
Jurac, S., McGrath, M. A., Johnson, R. E., Richardson, J. D., Vasyliunas, V. M., & Eviatar, A. (2002). Saturn: Search for a missing water source. *Geophysical Research Letters*, *29*(24), 2172. https://doi.org/10.1029/2002GL015855
Kanani, S. J., Arridge, C. S., Jones, G. H., Fazakerley, A. N., McAndrews, H. J., Sergis, N., et al. (2010). A new form of Saturn's magnetopause using a dynamic pressure balance model, based on in situ, multi-instrument Cassini measurements. *Journal of Geophysical Research*, *115*, A06207. https://doi.org/10.1029/2009JA014262
Kasper, J. C., Stevens, M. L., Lazarus, A. J., Steinberg, J. T., & Ogilvie, K. W. (2007). Solar wind helium abundance as a function of speed and heliographic latitude: Variation through a solar cycle. *The Astrophysical Journal*, *660*(1), 901.
Khurana, K. K. (2001). Influence of solar wind on Jupiter's magnetosphere deduced from currents in the equatorial plane. *Journal of Geophysical Research*, *106*(A11), 25,999–26,016. https://doi.org/10.1029/2000JA000352
Kivelson, M. G., & Southwood, D. J. (2005). Dynamical consequences of two modes of centrifugal instability in Jupiter's outer magnetosphere. *Journal of Geophysical Research*, *110*, A12209. https://doi.org/10.1029/2005JA011176
Krimigis, S. M., Sarris, E. T., Mitchell, D. G., Hamilton, D. C., Bertucci, C., & Dougherty, M. (2005). Spatial distribution, composition and charge state of energetic ions upstream from the Kronian magnetosphere. *Eos Trans. AGU 86(52), Fall Meet. Suppl. Abstract SH53B-08*.
Krimigis, S. M., Sergis, N., Mitchell, D. G., Hamilton, D. C., & Krupp, N. (2007). A dynamic, rotating ring current around Saturn. *Nature*, *450*(7172), 1050–1053.
Lanzerotti, L., Armstrong, T., Maclennan, C., Simnett, G., Cheng, A., Gold, R., et al. (1993). Special issue: Ulysses flyby of Jupiter measurements of hot plasmas in the magnetosphere of Jupiter. *Planetary and Space Science*, *41*(11), 893–917. https://doi.org/10.1016/0032-0633(93)90096-K
Luhmann, J. G., Johnson, R. E., Tokar, R. L., Ledvina, S. A., & Cravens, T. E. (2005). A model of the ionosphere of Saturn's rings and its implications. *AAS/Division for Planetary Sciences Meeting Abstracts #37, Bulletin of the American Astronomical Society* (Vol. 37, p. 758).
Martens, H. R., Reisenfeld, D. B., Williams, J. D., Johnson, R. E., & Smith, H. T. (2008). Observations of molecular oxygen ions in Saturn's inner magnetosphere. *Geophysical Research Letters*, *35*, L20103. https://doi.org/10.1029/2008GL035433
Mauk, B. H., Hamilton, D. C., Hill, T. W., Hospodarsky, G. B., Johnson, R. E., Paranicas, C., et al. (2009). Fundamental plasma processes in Saturn's magnetosphere. In M. K. Dougherty, L. W. Esposito, & S. M. Krimigis (Eds.), *Saturn from Cassini-Huygens* (pp. 281–331). Netherlands: Springer.
McAndrews, H., Thomsen, M., Arridge, C., Jackman, C., Wilson, R., Henderson, M., et al. (2009). Plasma in Saturn's nightside magnetosphere and the implications for global circulation. *Planetary and Space Science*, *57*(14–15), 1714–1722. https://doi.org/10.1016/j.pss.2009.03.003
McComas, D. J., Allegrini, F., Bagenal, F., Ebert, R. W., Elliott, H. A., Nicolaou, G., et al. (2017). Jovian deep magnetotail composition and structure. *Journal of Geophysical Research: Space Physics*, *122*, 1763–1777. https://doi.org/10.1002/2016JA023039
Paranicas, C., Roussos, E., Krupp, N., Kollmann, P., Hendrix, A. R., Cassidy, T., et al. (2012). Energetic charged particle weathering of Saturn's inner satellites. *Planetary and Space Science*, *61*(1), 60–65. https://doi.org/10.1016/j.pss.2011.02.012

Persoon, A. M., Gurnett, D. A., Santolik, O., Kurth, W. S., Faden, J. B., Groene, J. B., et al. (2009). A diffusive equilibrium model for the plasma density in Saturn's magnetosphere. *Journal of Geophysical Research*, *114*, A04211. https://doi.org/10.1029/2008JA013912

Pilkington, N. M., Achilleos, N., Arridge, C. S., Guio, P., Masters, A., Ray, L. C., et al. (2015). Asymmetries observed in Saturn's magnetopause geometry. *Geophysical Research Letters*, *42*, 6890–6898. https://doi.org/10.1002/2015GL065477

Reisenfeld, D., Williams, J., Baragiola, R., Fama, M., Martens, H., Sittler, E., et al. (2008). The ion composition of Saturn's magnetosphere. *37th COSPAR Scientific Assembly, COSPAR Meeting* (Vol. 37, p. 2593).

Richardson, J. D., & Jurac, S. (2004). A self-consistent model of plasma and neutrals at Saturn: The ion tori. *Geophysical Research Letters*, *31*, L24803. https://doi.org/10.1029/2004GL020959

Sergis, N., Arridge, C. S., Krimigis, S. M., Mitchell, D. G., Rymer, A. M., Hamilton, D. C., et al. (2011). Dynamics and seasonal variations in Saturn's magnetospheric plasma sheet, as measured by Cassini. *Journal of Geophysical Research*, *116*, A04203. https://doi.org/10.1029/2010JA016180

Sittler, E., Andre, N., Blanc, M., Burger, M., Johnson, R., Coates, A., et al. (2008). Ion and neutral sources and sinks within saturn's inner magnetosphere: Cassini results. *Planetary and Space Science*, *56*(1), 3–18. https://doi.org/10.1016/j.pss.2007.06.006, surfaces and Atmospheres of the Outer Planets, their Satellites and Ring Systems: Part III.

Smith, A. W., Jackman, C. M., & Thomsen, M. F. (2016). Magnetic reconnection in Saturn's magnetotail: A comprehensive magnetic field survey. *Journal of Geophysical Research: Space Physics*, *121*, 2984–3005. https://doi.org/10.1002/2015JA022005

Thomsen, M. F. (2013). Saturn's magnetospheric dynamics. *Geophysical Research Letters*, *40*, 5337–5344. https://doi.org/10.1002/2013GL057967

Thomsen, M. F., DiLorenzo, J. P., McComas, D. J., Young, D. T., Crary, F. J., Delapp, D., et al. (2007). Assessment of the magnetospheric contribution to the suprathermal ions in Saturn's foreshock region. *Journal of Geophysical Research*, *112*, A05220. https://doi.org/10.1029/2006JA012084

Thomsen, M. F., Jackman, C. M., Tokar, R. L., & Wilson, R. J. (2014). Plasma flows in Saturn's nightside magnetosphere. *Journal of Geophysical Research: Space Physics*, *119*, 4521–4535. https://doi.org/10.1002/2014JA019912

Thomsen, M. F., Reisenfeld, D. B., Delapp, D. M., Tokar, R. L., Young, D. T., Crary, F. J., et al. (2010). Survey of ion plasma parameters in Saturn's magnetosphere. *Journal of Geophysical Research*, *115*(A10) A10220. https://doi.org/10.1029/2010JA015267

Thomsen, M. F., Roussos, E., Andriopoulou, M., Kollmann, P., Arridge, C. S., Paranicas, C. P., et al. (2012). Saturn's inner magnetospheric convection pattern: Further evidence. *Journal of Geophysical Research*, *117*, A09208. https://doi.org/10.1029/2011JA017482.

Tokar, R. L., Johnson, R. E., Hill, T. W., Pontius, D. H., Kurth, W. S., Crary, F. J., et al. (2006). The interaction of the atmosphere of Enceladus with Saturn's plasma. *Science*, *311*, 1409–1412. https://doi.org/10.1126/science.1121061

Tokar, R. L., Johnson, R. E., Thomsen, M. F., Delapp, D. M., Baragiola, R. A., Francis, M. F., et al. (2005). Cassini observations of the thermal plasma in the vicinity of Saturn's main rings and the F and G rings. *Geophysical Research Letters*, *32*, L14S04. https://doi.org/10.1029/2005GL022690

Tseng, W. L., Ip, W. H., Johnson, R. E., Cassidy, T. A., & Elrod, M. K. (2010). The structure and time variability of the ring atmosphere and ionosphere. *Icarus*, *206*(2), 382–389. https://doi.org/10.1016/j.icarus.2009.05.019

Tseng, W.-L., Johnson, R., & Elrod, M. (2013). Modeling the seasonal variability of the plasma environment in Saturn's magnetosphere between main rings and Mimas. *Planetary and Space Science*, *77*, 126–135. https://doi.org/10.1016/j.pss.2012.05.001

Tseng, W.-L., Johnson, R. E., Thomsen, M. F., Cassidy, T. A., & Elrod, M. K. (2011). Neutral H2 and H2+ ions in the Saturnian magnetosphere. *Journal of Geophysical Research*, *116*, A03209. https://doi.org/10.1029/2010JA016145

Vasyliunas, V. M. (1983). Plasma distribution and flow, *Physics of the Jovian Magnetosphere* (pp. 395–453). Cambridge and New York: Cambridge University Press.

Vasyliunas, V. M. (2008). Comparing Jupiter and Saturn: Dimensionless input rates from plasma sources within the magnetosphere. *Annales Geophysicae*, *26*(6), 1341–1343. https://doi.org/10.5194/angeo-26-1341-2008

Waite, J. H., Combi, M. R., Ip, W.-H., Cravens, T. E., McNutt, R. L., Kasprzak, W., et al. (2006). Cassini ion and neutral mass spectrometer: Enceladus plume composition and structure. *Science*, *311*(5766), 1419–1422. https://doi.org/10.1126/science.1121290

Wang, Y. M. (2008). Relating the solar wind helium abundance to the coronal magnetic field. *The Astrophysical Journal*, *683*(1), 499.

Wilson, R. J., Bagenal, F., Cassidy, T., Fleshman, B. L., & Crary, F. (2015). The relative proportions of water group ions in Saturn's inner magnetosphere: A preliminary study. *Journal of Geophysical Research: Space Physics*, *120*, 6624–6632. https://doi.org/10.1002/2014JA020557

Wilson, R. J., Bagenal, F., Delamere, P. A., Desroche, M., Fleshman, B. L., & Dols, V. (2013). Evidence from radial velocity measurements of a global electric field in Saturn's inner magnetosphere. *Journal of Geophysical Research: Space Physics*, *118*, 2122–2132. https://doi.org/10.1002/jgra.50251

Wilson, R. J., Crary, F., Gilbert, L. K., Reisenfeld, D. B., Steinberg, J. T., & Livi, R. (2012). *PDS User's Guide for Cassini Plasma Spectrometer*. Retrieved from http://ppi.pds.nasa.gov/

Young, D., Berthelier, J., Blanc, M., Burch, J., Coates, A., Goldstein, R., et al. (2004). Cassini plasma spectrometer investigation. In C. Russell (Ed.), *The Cassini-Huygens Mission* (pp. 1–112). Netherlands: Springer. https://doi.org/10.1007/978-1-4020-2774-1_1